# NEAR-FIELD DISPERSAL MODELING FOR LIQUID FUEL-AIR EXPLOSIVES

David R. Gardner
Severe Accident Phenomenology Division
Sandia National Laboratoraies
Albuquerque, NM 87185

SAND--90-0686

DE91 000079

## ABSTRACT

The near-field, explosive dispersal of a liquid into air has been
explored using a combination of analytical and numerical models. The
near-field flow regime is transient, existing only as long as the
explosive forces produced by the detonation of the burster charge
dominate or are approximately equal in magnitude to the aerodynamic drag
forces on the liquid. The near-field model provides reasonable initial
conditions for the far-field model, which is described in a separate
report. The near-field model consists of the CTH hydrodynamics code and
a film instability model. In particular, the CTH hydrodynamics code is
used to provide initial temperature, pressure, and velocity fields, and
bulk material distribution for the far-field model. The film
instability model is a linear stability model for a radially expanding
fluid film, and is used to provide a lower bound on the breakup time and
an upper and lower bound on the initial average drop diameter for the
liquid following breakup. Predictions of the liquid breakup time and
the initial arithmetic average drop diameter from the model compare
favorably with the sparse experimental data.

**MASTER**

# TABLE OF CONTENTS

# LIST OF FIGURES

# LIST OF FIGURES
## (continued)

## LIST OF FIGURES
### (continued)

# LIST OF TABLES

# 1. INTRODUCTION

A fuel-air explosive device mixes a liquid or solid fuel with air to produce a detonable mixture. The archetypical fuel-air explosive device is cylindrical, with a central, cylindrical burster charge surrounded by a cylindrical annulus of liquid fuel. When the central burster charge is detonated, the casing is fragmented, and the fuel is propelled explosively outward and breaks into drops. Further expansion and turbulent mixing create an aerosol cloud that is roughly toroidal in shape. Detonating the resulting cloud with a second high explosive charge can produce a blast wave which can inflict considerable damage on blast-sensitive targets such as buildings and vehicles.

Current fuel-air explosive devices use liquid fuels with high vapor pressures. Such fuels pose a significant safety hazard, as leaking fuel can evaporate and form a detonable fuel-air mixture in a confined space (such as on board a ship). Such devices thus require hypergolic storage, which limits their availability and utility.

Low vapor pressure liquid fuels and solid fuels, and slurried and gelled fuels promise greater safety, if they can be reliably detonated after dispersal.

Improving the reliability of detonation of a fuel-air cloud depends on understanding the mechanisms important in the detonation of aerosols. This includes understanding the mechanism(s) of fuel dispersal and consequently which factors influence the final cloud shape and fuel distribution produced by dispersal from a given device.

The blast yield is a function of fuel-air reaction chemistry, which depends on the physical state of the fuel including particle size and concentration. The latter are determined by the dispersal process.

Thus the outcome of the dispersal process impacts the reliability of detonation of the fuel-air cloud, and also the blast yield. Consequently, an understanding of the process of explosive dispersal is important in designing improved fuel-air explosive devices.

The Enhanced Blast Munitions Program has addressed how to provide the technology base that would enable the design and development of safe, reliable, high-yield, and high-efficiency blast weapons based on fuel-air explosives. Within that program, the goal of the dispersal modeling work was to create a model to simulate the formation of a fuel-air

aerosol cloud, from the initial device to the point of detonation of the fuel-air cloud. Ultimately, the model was intended to include liquid and solid fuels, and devices of various sizes and shapes.

The process of explosive dispersal can be divided into three regimes, based on the relative magnitudes of the explosive and aerodynamic forces acting on the fuel [1]. In the ejection regime, explosive forces from the detonation of the burster charge dominate the aerodynamic forces. This regime is succeeded by the transition regime, in which the explosive and aerodynamic forces are of approximately equal magnitude. In both the ejection and transition regimes, the fuel concentration in the evolving cloud is relatively high and strong shock waves reverberate through the cloud. The transition regime is succeeded by the expansion regime, in which aerodynamic forces dominate the explosive forces, the fuel concentration in the cloud is relatively low, and the shock waves have decayed to insignificance.

Previous dispersal modeling efforts for fuel-air explosives have included both linear-regressions of vast amounts of experimental data (e.g., [1, 2, 3]), and numerical solutions to the Navier-Stokes equations (e.g., [3, 4, 5]). However, none of these previous efforts modeled the entire dispersal process, and in particular no attempt was made to model the initial breakup of liquids into drops [6].

For the purposes of our dispersal modeling effort, the ejection and transition regimes described above were combined into a regime called the near-field regime. This definition reflects the fact that less is known about the physical processes occurring in the ejection and transition regimes than in the expansion regime. To complement the new terminology, the expansion regime was renamed the far-field regime.

The general approach employed in our dispersal modeling effort in each of the near-field and far-field regimes was to

  • use existing numerical tools where possible,

  • consider solid and liquid fuels separately, and

  • endeavor to understand the underlying physics.

Consonant with this general approach, and early in the dispersal modeling effort, the KIVA hydrodynamics code [7-10] was selected as the

far-field modeling tool. KIVA is a one-, two-, or three-dimensional finite difference code for modeling transient fluid flows with chemically-reacting fuel sprays. The fuel drops are modeled stoichastically, using parcels to represent a number of physical particles with identical properties. The desired initial drop size distribution can be chosen by the user. KIVA incorporates models for the evaporation, aerodynamic breakup, collision and coalescence, and turbulent motion of liquid fuel drops. It also incorporates both a k-ε turbulence model and a subgrid turbulence model. (Although turbulence models are not well-developed for compressible flows in unconfined geometries, the presence of these models in KIVA was considered sufficient for the initial phases of the development of the dispersal models.) Hence it was considered to be a good choice for simulating the formation of aerosol clouds.

However, KIVA is inaccurate for large fuel concentrations, and is unable to model well the strong shock waves present during the near-field regime of the dispersal process.

In the context of our dispersal modeling work, the near-field regime extends in time from the detonation of the burster charge in the fuel-air device to a time when the average fuel concentration in the developing aerosol cloud is small enough and the shock waves from the burster charge are weak enough for KIVA to be a valid model. The near-field regime thus includes the processes of

- fragmentation of the outer canister enclosing the fuel,

- the early expansion of the fuel as a coherent shell, and

- the breakup of the shell into a field of drops.

The spatial extent of the near-field regime depends on the device dimensions. A conservative estimate of the maximum radial extent of the near-field regime, based on concentration only, is shown in Figure 1, as a function of the outer radius of the device. The radial extent of the near-field regime is over-estimated in Figure 1. This figure shows the estimated outer radius of the fuel air cloud at the time when the near-field regime vanishes.

This report describes the near-field dispersal modeling effort. The far-field dispersal modeling effort is described in [23]. The coupled near-field, far-field model is described in [22].
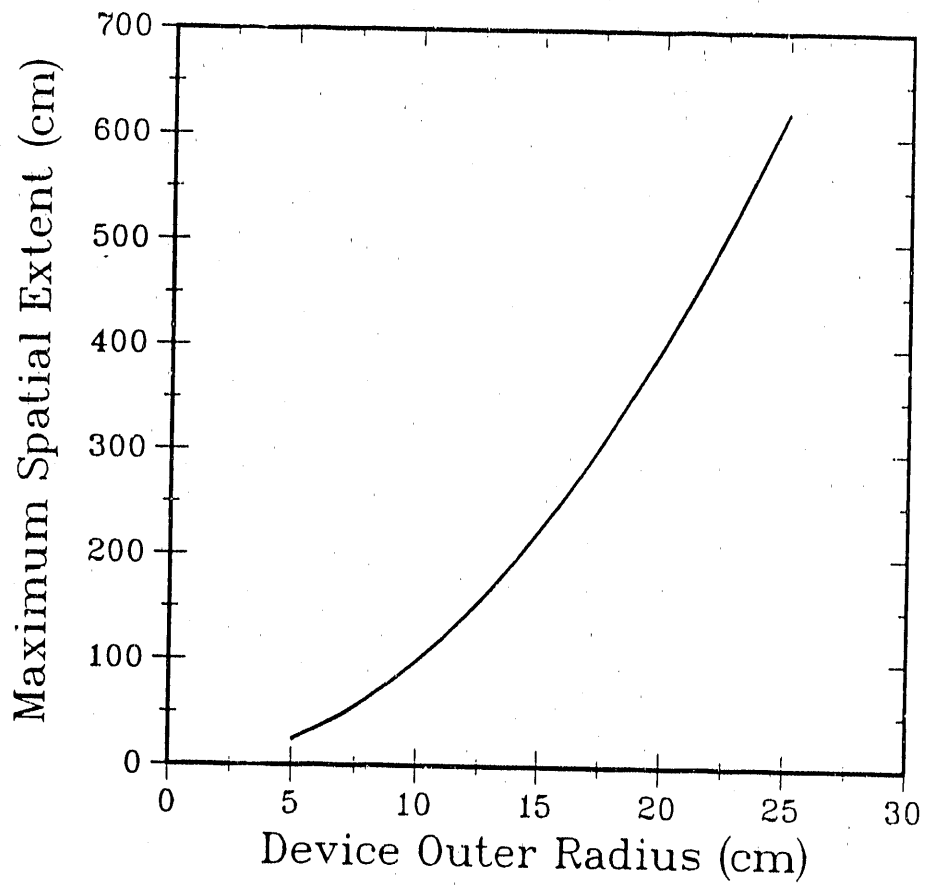
Figure 1: The maximum radial extent of the near-field regime increases
with increasing dimensions of a fuel-air explosive device
(initial device inner radius = 1 cm).

The goal of the near-field modeling effort is to provide reasonable initial conditions for the far-field model. This includes specifying appropriate initial

- temperature fields,

- pressure fields,

- velocity fields,

- bulk material distributions,

- average particle sizes, and

- particle size distributions.

Modeling of formation of the fuel-air aerosol cloud is hindered by the sparsity of reliable experimental data. Most of the data reported in the literature are the average rate of cloud growth (radius and height, or volume) for various fuels and sizes and geometries of devices. Various attempts have been made to measure particle sizes in fuel-air clouds, but with mixed success [1, 3, 11, 12, 13, 14]. Almost all the data available are for the fully developed cloud (*i.e.*, in the far-field regime, as defined here). The only data available for the near-field regime were reported by Samirant *et al.* [12].

The numerical model used to predict the temperature, pressure, and velocity fields, and the bulk material distribution, will be described first. Next the complementary analytical model will be described; this model was developed to predict the liquid breakup time and the arithmetic average drop diameter at breakup. The resulting combined near-field model will be illustrated, and recommendations for further work will be discussed. Some details of the analytical model are presented in Appendix 4, and two energy-based breakup models are discussed in Appendices 2 and 3.

## 2. NUMERICAL MODELS

Numerical modeling of the breakup of a mass of liquid into a field of drops is intrinsically difficult, owing to

- the many length scales involved,

- the important role played by interfacial physics,

- the need to track the location of material phases, and

- the requirement that the physics of liquids and their vapors be treated simultaneously.

These factors place stringent limitations on any numerical modeling tools used to simulate the explosive breakup of a liquid.

The presence of multiple length scales complicates any numerical simulation because all the significant length scales must be adequately resolved. In a finite difference code, very fine computational grids are required. This greatly reduces the maximum allowed time step for any explicit solution scheme, and hence greatly increases computation costs.

When the bulk liquid breaks up into a field of drops, there is an enormous increase in the ratio of surface area to volume for the liquid. Interfacial effects can no longer be ignored, *i.e.*, surface tension becomes important. Certainly the representation of the surfaces becomes very important. This places several constraints on any numerical simulation tool that is to be used to simulate liquid breakup:

- there must be little numerical diffusion, so that simulated interfaces remain distinct,

- there must be an accurate representation of the interface, and

- surface tension must be modeled correctly.

The requirement of little numerical diffusion restricts the types of solution algorithms that can be used. The requirement for a good representation of the interface requires that some appropriate interface tracker be used. Surface tension is not modeled well in most hydrodynamics codes.

As the shock waves from the detonation of the central high explosive burster charge reverberate in the liquid mass, some of the liquid may vaporize [13]. Hence regions of a liquid and its vapor must be tracked independently. This is difficult to do, especially on the fine scales of cavitation seen in explosively dispersed liquids, and is not done in most hydrodynamics codes.

In addition, the coexistence of regions of condensed liquid and vapor presents problems for many hydrodynamics codes. Codes that work well for incompressible fluids may not work well at all for compressible ones, and vice versa.

Consonant with the strategy of using existing computational tools where possible, a survey of existing numerical tools was conducted. The survey included two- and three-dimensional codes, Lagrangian, Eulerian, and arbitrary Lagrangian-Eulerian (ALE) codes, vortex codes, particle-in-cell (PIC) codes, free-Lagrangian codes, finite difference codes, and finite element codes. Codes and algorithms were evaluated on the basis of the criteria discussed above.

Following this survey, the CTH [15] hydrodynamics code was selected because

- it was readily available,

- there was little evidence of numerical diffusion in test simulations of the dispersal of a liquid into air,

- an explicit interface tracker is employed,

- sophisticated equations of state can be employed, and

- detonations of high explosives can be simulated.

The CTH hydrodynamics code is an Eulerian finite difference code which uses a van Leer monotonic advection scheme that is formally second-order accurate. It can model multi-dimensional, multi-material shock-wave physics. Simulations can be performed in one-, two-, or three-spatial dimensions, thus allowing the simulation of fuel-air explosive devices of various shapes. Models are included for treating the strength, fracture, and distension of various materials, and the detonation of high-explosives.

CTH lacks any model for surface tension; however, this was true for most codes included in the survey.

A typical dispersal simulation is shown in Figures 2-7 for liquid decane being dispersed into air by a cylindrical device. The central burster charge is the high explosive PBX9010 and the fuel mass to burster mass ratio was 100:1. The initial dimensions of one quarter of the model device are given in Figure 2. The CTH input files used to generate this simulation are presented in Appendix 1. This simulation models the liquid-fuel jug tests conducted at the Naval Weapons Center, China Lake, CA. Decane was chosen to represent transportation fuels, some of which were considered as fuels for improved fuel-air explosives.

In each of Figures 2-7 only one quarter of the symmetrical problem domain is shown. The full domain is obtained by reflecting the region shown in both the axial and radial axes.

Figure 3 shows the evolution of the material interfaces from 0 to 2 msec. The decane expands radially and axially as a more or less coherent film. (The axial expansion could be inhibited by placing a metal plate on top of the device, instead of using a metal plug. This is often done in jug tests at the Naval Weapons Center, China Lake, CA.) The isopycnics (constant density contours) at 2 msec are shown in Figure 4. Although they suggest that the liquid decane is not a coherent film, this is a computational artifact resulting from the finite size of the computational cells.

In Figure 5, the steep thermal gradient across the decane film at 2 msec is evident. The temperature changes from approximately 1800 K at the inner surface of the film (adjacent to the detonation product gases) to 300 K at the outer surface of the film, over a distance on the order of 1 cm.

Figure 6 indicates that the pressure of the detonation product gases is less than ambient at 2 msec; the cloud continues to expand outward due to inertia. This is seen by the velocity vectors at 2 msec in Figure 7 in which incipient vortices are visible.

CTH is suitable for simulating the temperature, pressure, and velocity fields, and the bulk material distribution in the explosive dispersal of a liquid. However, owing to the absence of a surface tension model, it is unable to provide much useful information regarding the breakup of the liquid into drops: the time of breakup or the arithmetic average drop diameter immediately after breakup. Analytical models were investigated to remedy this deficiency.
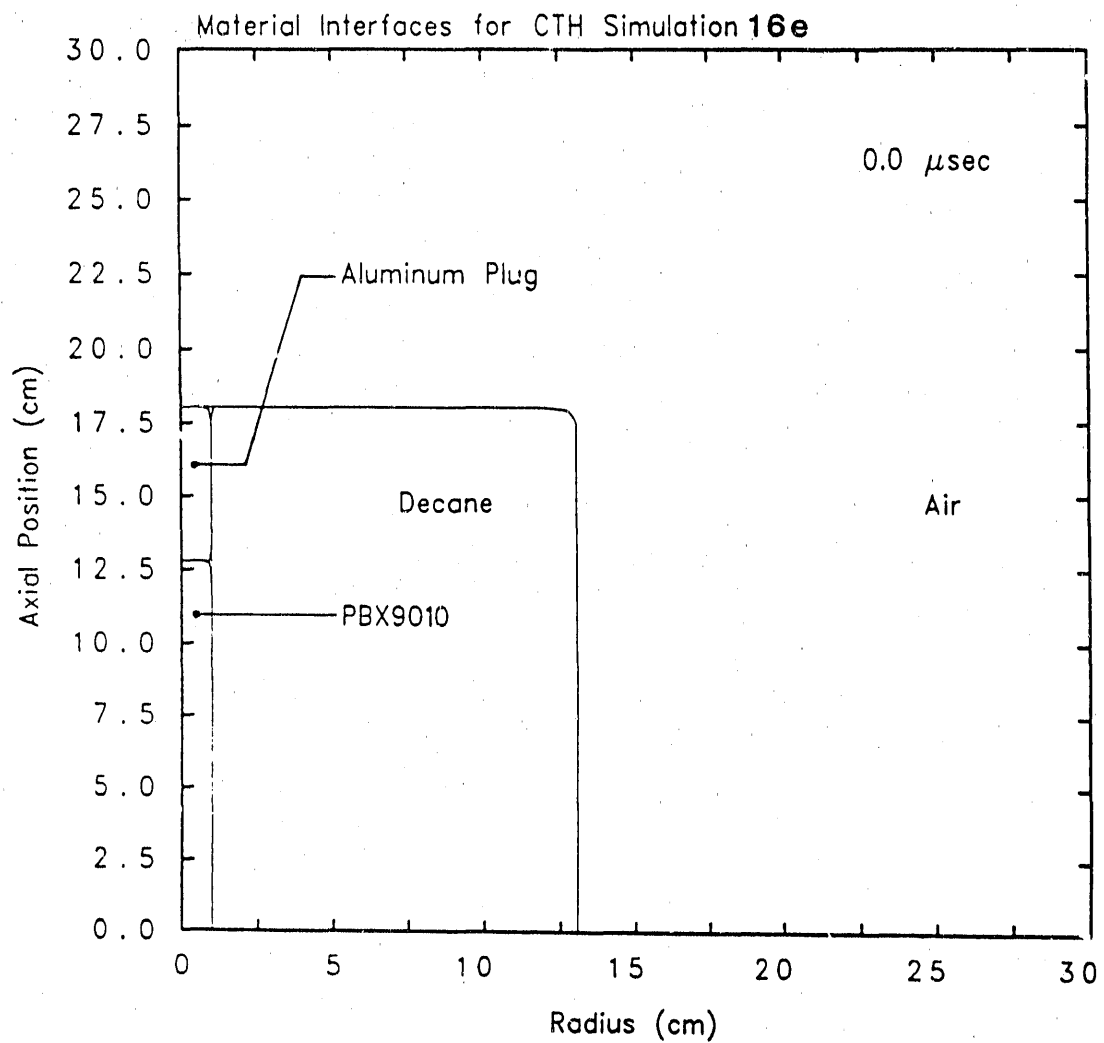
Figure 2:    (a)  The initial geometry and dimensions for the fuel-air
             explosive device used in a CTH simulation of the dispersal
             of decane into air.
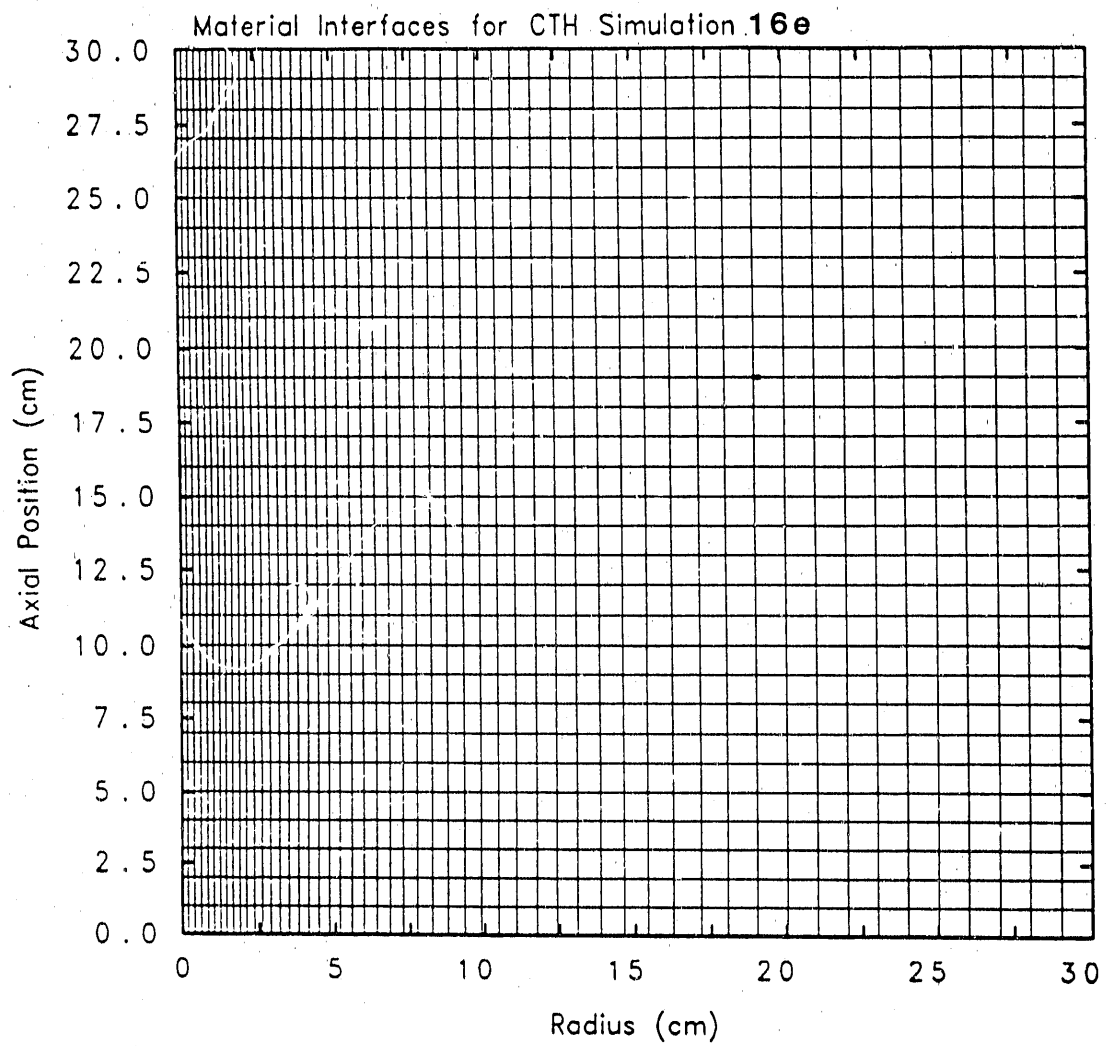
Figure 2, continued:   (b)   The initial computational grid.

Material Interfaces for CTH Simulation 16e

250 μsec

Air

Gaseous Explosive Products

Liquid Decane



Material Interfaces for CTH Simulation 16e

500 μsec

Air

Liquid Decane

Gaseous Explosive Products
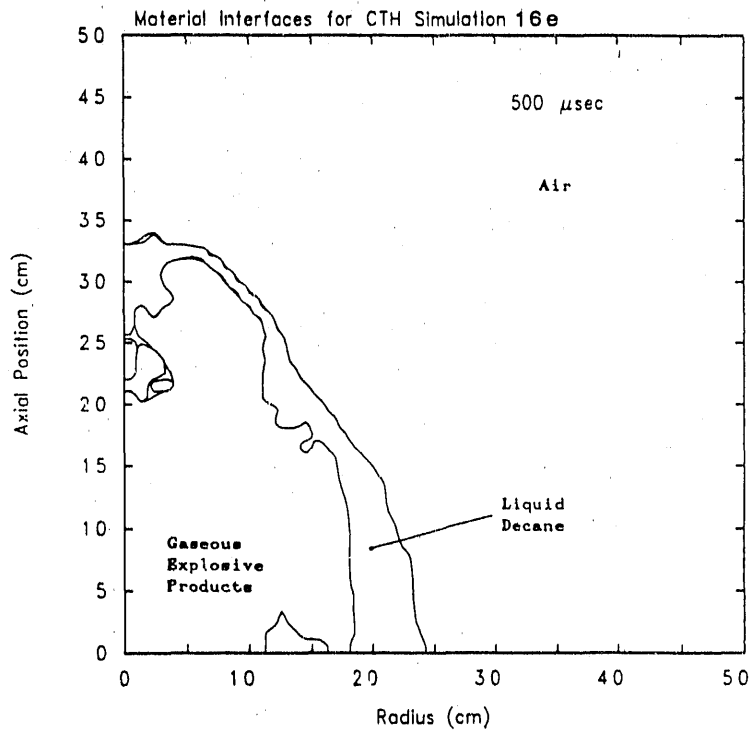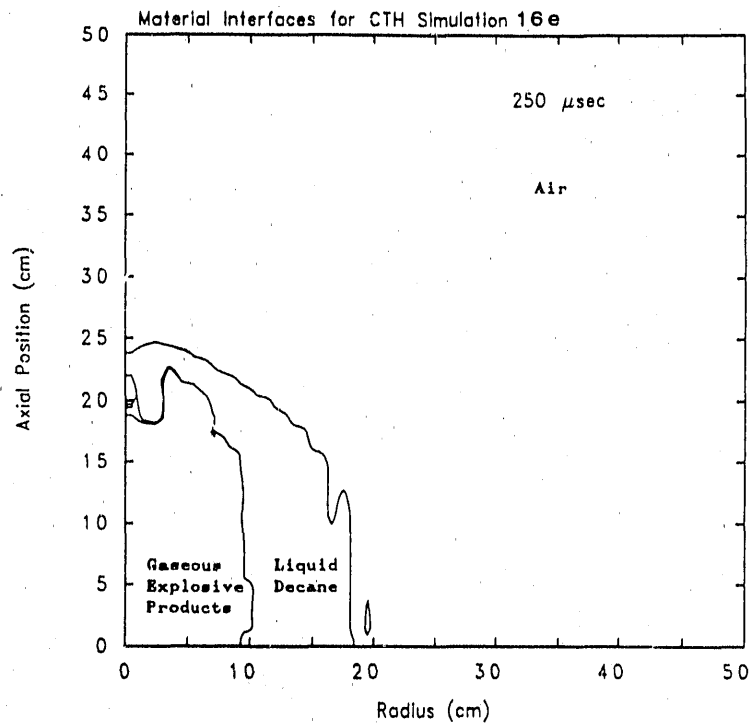
Figure 3:   Evolution of the material interfaces in a CTH simulation of the dispersal of decane into air, at times of (a) 0.25 msec, (b) 0.50 msec.

- 11 -
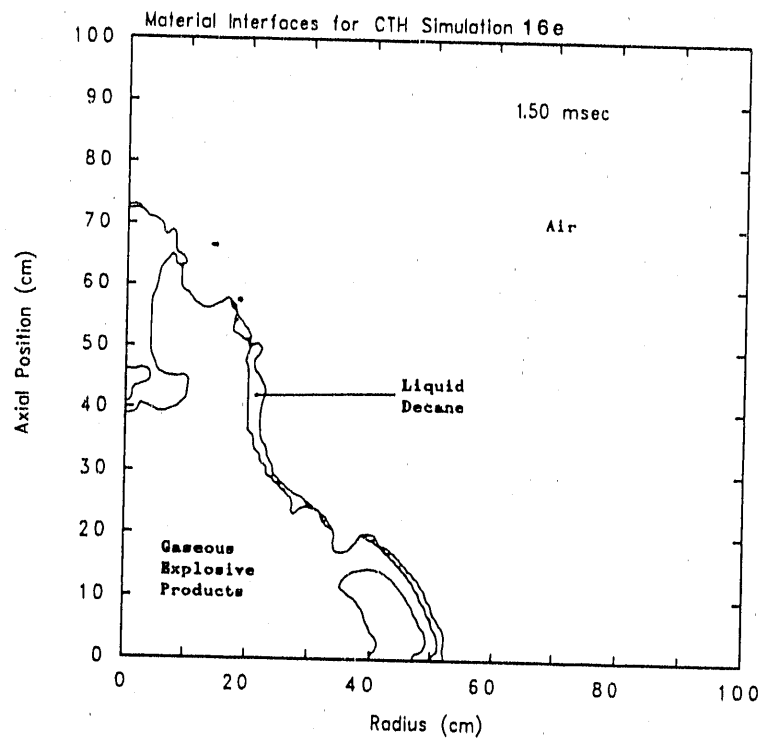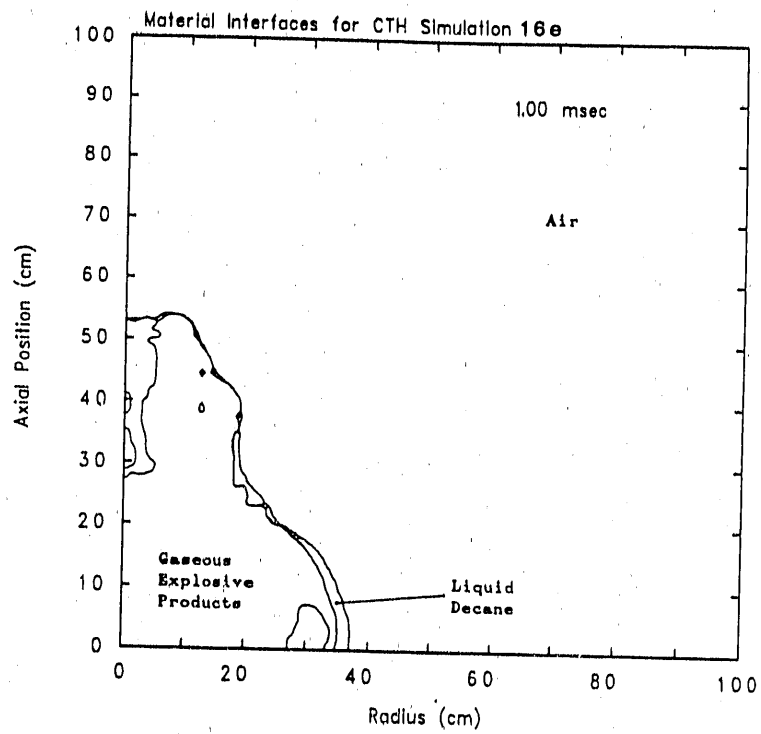
Figure 3, continued:   (c) 1.0 msec, and (d) 1.5 msec.
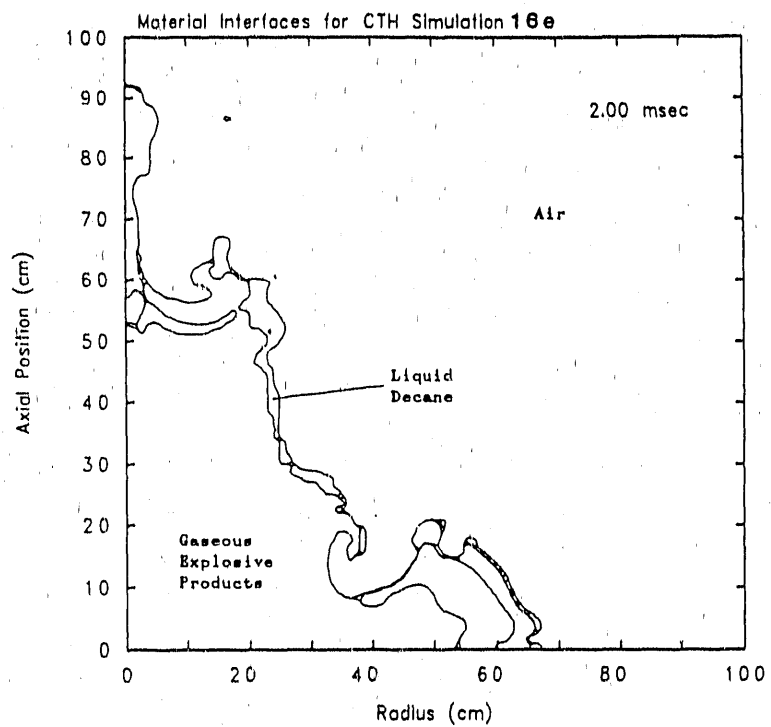
Figure 3, continued:  (e) 2.0 msec.
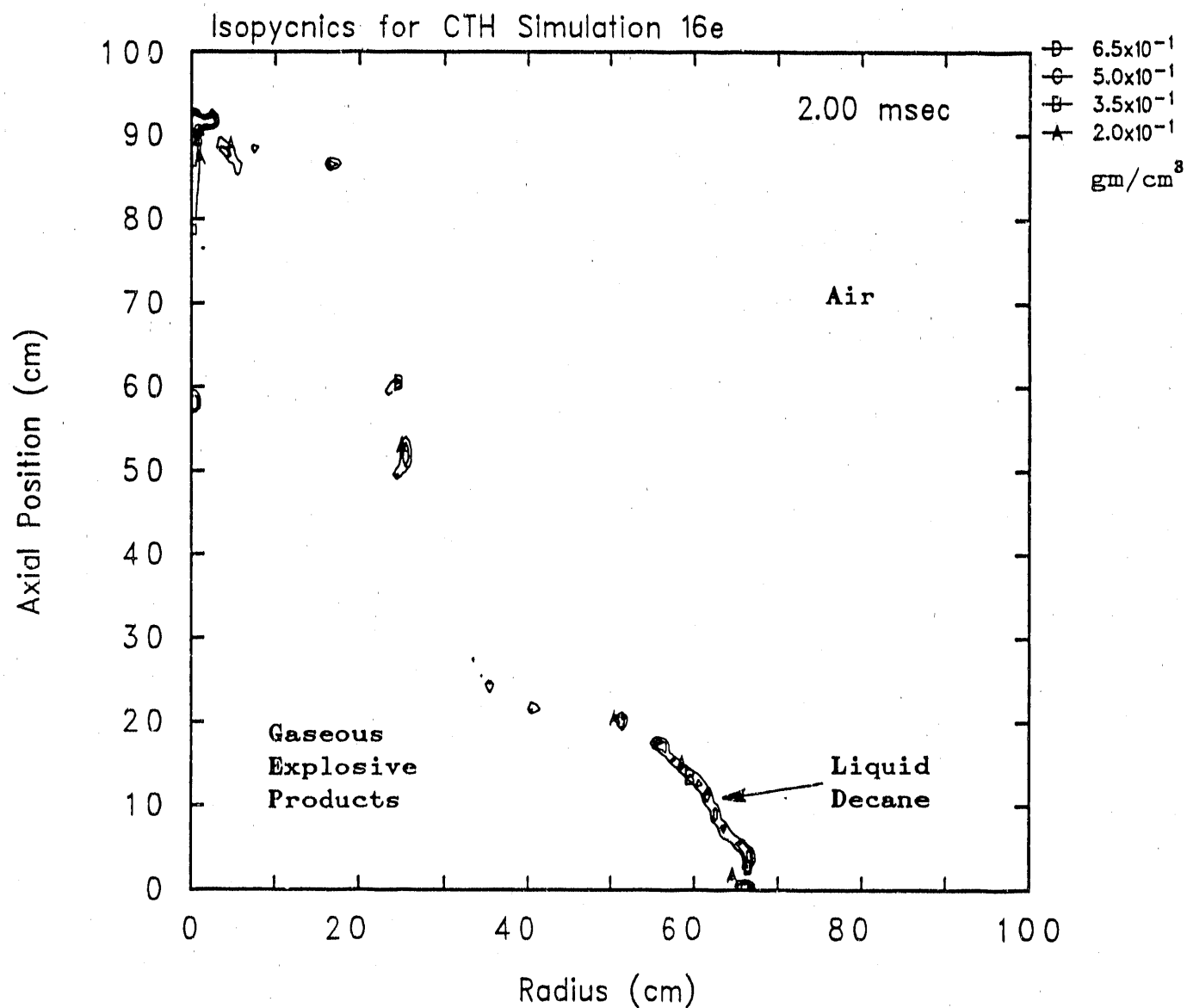
Figure 4:   Isopycnics (constant density contours) for a CTH simulation
            of the dispersal of decane into air, at 2 msec.
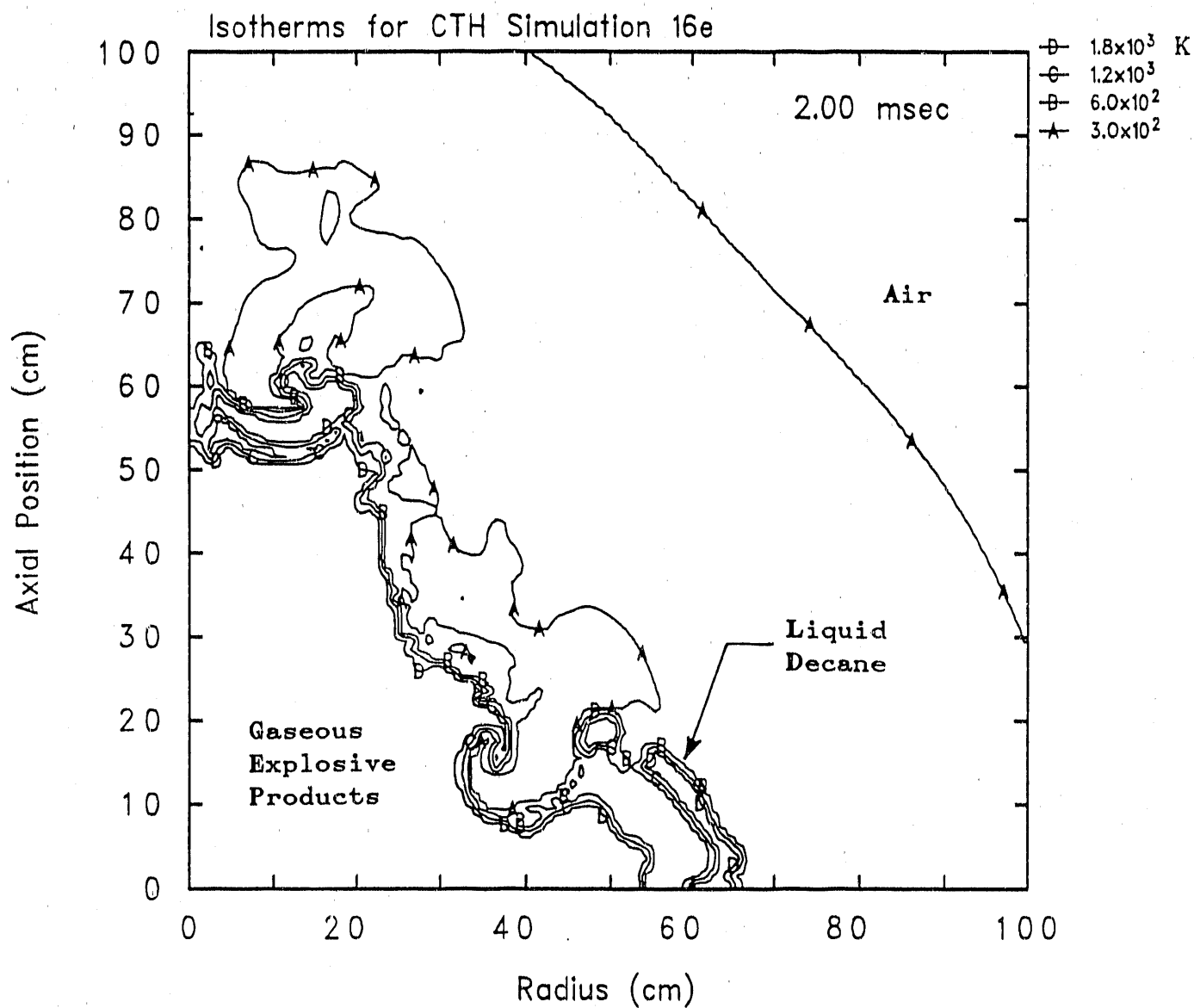
Figure 5:   Isotherms for a CTH simulation of the dispersal of decane
            into air, at 2 msec.
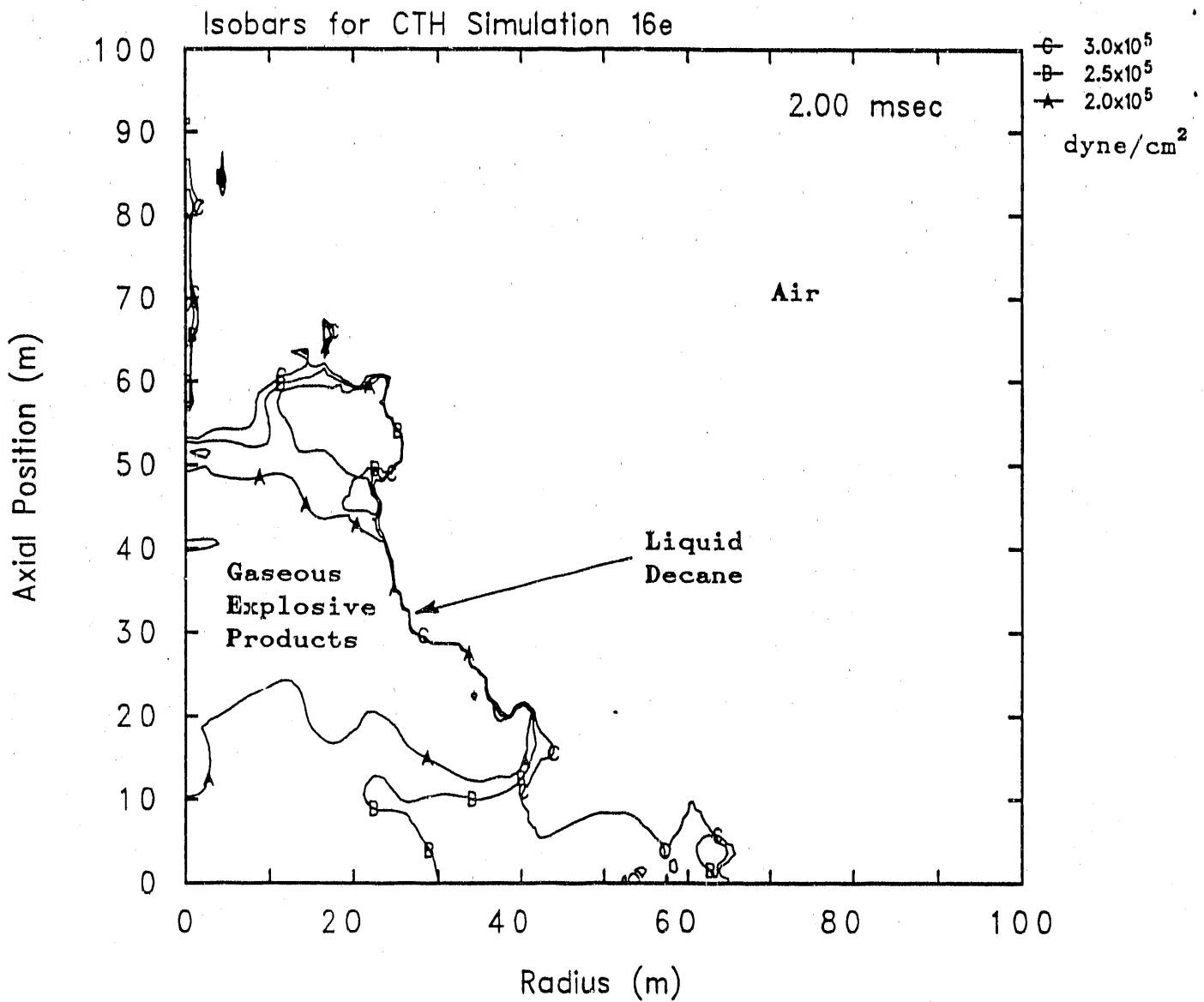
Figure 6:    Isobars for the CTH simulation of the dispersal of decane
             into air, at 2 msec.

Velocity Vectors for CTH Simulation 16e

Axial Position (cm)

100

90

80

70

60

50

40

30

20

10

0

2.00 msec

5.0e+04
cm/sec

Air

Gaseous

Explosive
Products

Liquid
Decane

0        20        40        60        80        100

Radius (cm)
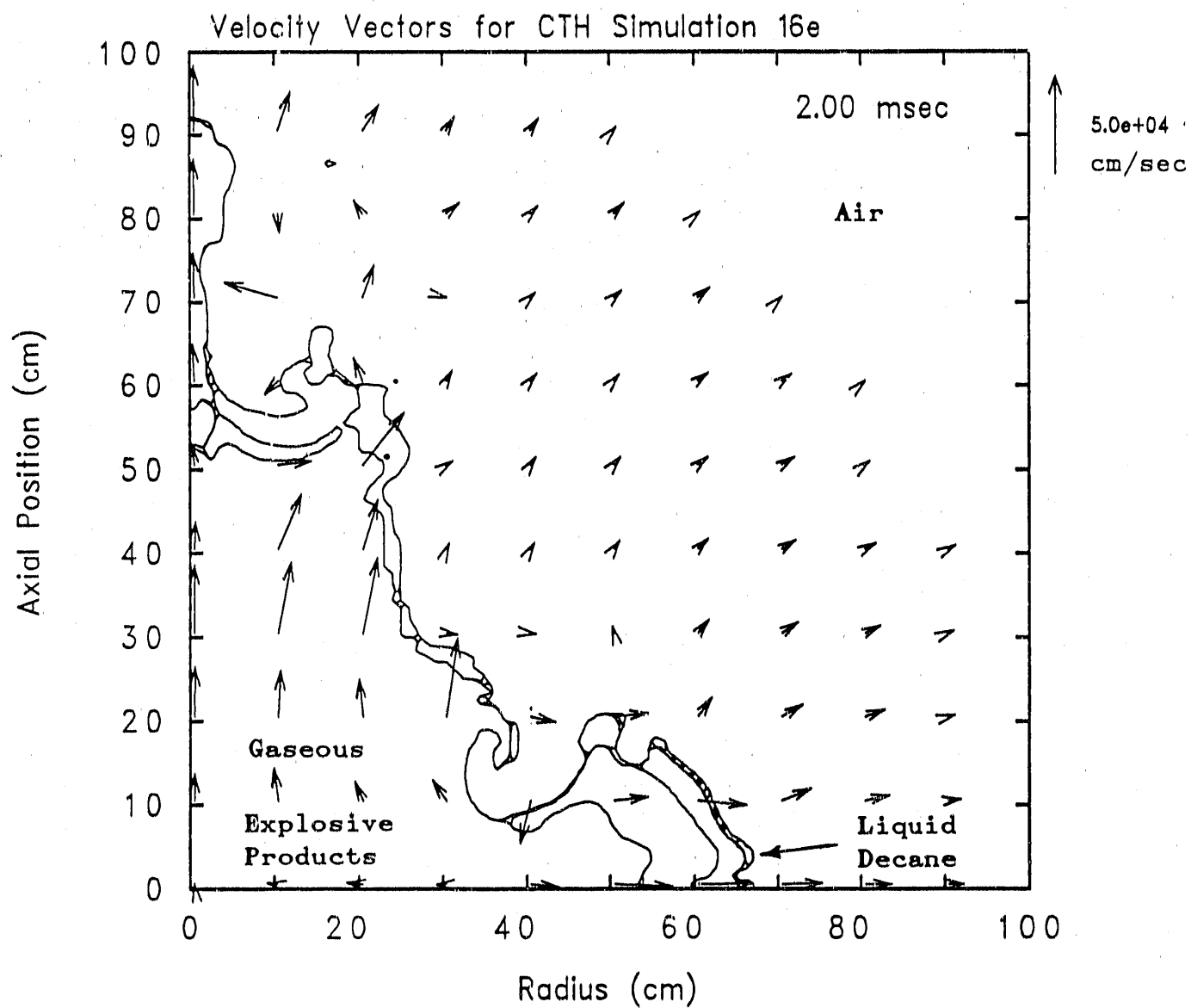
Figure 7:    Velocity vectors for a CTH simulation of the dispersal of
decane into air, at 2 msec.

# 3. ANALYTICAL MODELS

Owing to the difficulties discussed above, existing numerical models are unable to provide useful estimates of the initial arithmetic average drop diameter in the explosive breakup of a mass of liquid. Thus several analytical models were explored to provide the necessary estimates. The analytical models will provide some useful bounds on the drop diameters.

Three analytical models were explored. The first model is a simple one based on minimizing surface energy. It provides estimates of either the breakup time (if the initial drop diameter is known) or the initial drop diameter (if the breakup time is known). This model is described in Appendix 2.

The second model is one devised by D. E. Grady [16-19]. It is also based on energy concepts. It provides estimates of both the breakup time and the initial arithmetic average drop diameter, and is described in Appendix 3. However, the model is based on the concept of liquid spall, which has not been experimentally observed [1, 20], and its predictions do not compare well with the (sparse) experimental data.

The third analytical model is based on the linear instability of a radially expanding fluid film. It provides estimates of the breakup time and the initial arithmetic average drop diameter. Owing to the assumptions made in constructing the model, it provides a lower bound on the breakup time, and both upper and lower bounds on the initial arithmetic average drop diameter. Its predictions compare favorably with the (sparse) experimental data, and hence it is the model recommended by this study.

The film instability model is described below.


## 3.1  Description of the Film Instability Model

The model presented here is based on the linear stability of a radially expanding fluid film. The model includes surface tension, but does not include viscosity.

Consider a cylinder of fluid, denoted fluid 1, of radius $R_i(t)$, where t represents time, and height $2z_\emptyset$. This is surrounded by an annulus of fluid, denoted fluid 2, of outer radius $R_o(t)$ and also of height $2z_\emptyset$.

Surrounding the annulus of fluid 2 is an infinite fluid medium denoted fluid 3. The interface between fluids 1 and 2 is denoted interface 1, and the interface between fluids 2 and 3 is denoted interface 2. A cross section of this arrangement is shown in Figure 8.

With reference to a fuel-air cloud, fluid 1 represents the detonation reaction product gases for the high explosive burster charge. Fluid 2 represents the liquid fuel to be dispersed. Fluid 3 represents the ambient atmosphere.

Let

- $\rho$ represent fluid density,
- R represent the radial spatial variable,
- t represent time,
- U represent the radial velocity component, and
- P represent pressure.

We non-dimensionalize using the following scales:

- $z_0$ for length,
- $V_o$ for velocity,
- $z_0/V_o$ for time, and
- $(\rho_1 + \rho_2 + \rho_3)V_o^2$ for pressures.

We also define the density ratios $\beta_i = \rho_i/(\rho_1 + \rho_2 + \rho_3)$.

This produces the non-dimensional variables

- r for radius,
- $\tau$ for time,
- u for the radial velocity component, and
- p for pressure.

The correspondence between dimensional and dimensionless variables is given in Table 1.

We assume that the fluids are inviscid and incompressible, and that the flow is purely radial, irrotational, and isothermal.
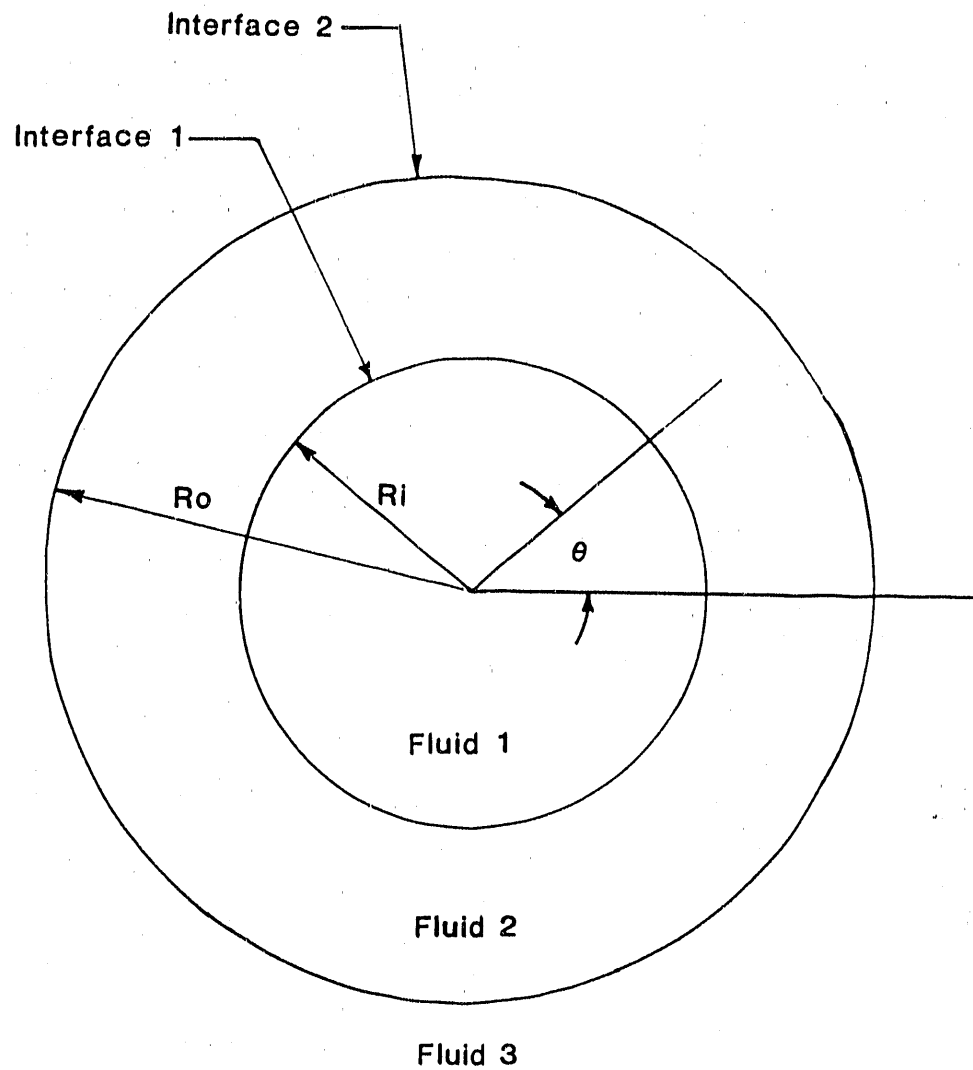
Figure 8: Cylindrical geometry used for the film instability model.

Although these assumptions are not valid in the expanding detonation reaction product gases, or in the surrounding atmosphere, they permit an analytical solution to be obtained. Predictions from this solution will provide useful bounds on the liquid breakup time and the initial drop diameter. These bounds can then be compared to the experimental data.

Table 1: Relationship between dimensional variables and parameters and dimensionless variables and parameters for the film instability model.

| Divide<br>Dimensional Variable | by<br>Scale | to Obtain<br>Dimensionless Variable |
|---|---|---|
| Radius, R | $z_0$ | $r$ |
| Radial Velocity, U | $V_o$ | $u$ |
| Time, t | $z_0/V_o$ | $\tau$ |
| Density, $\rho_i$ | $\rho_1 + \rho_2 + \rho_3$ | $\beta_i$ |
| Pressure, P | $(\rho_1 + \rho_2 + \rho_3)V_o^2$ | $p$ |
| Surface Tension, $\sigma$ | $(\rho_1 + \rho_2 + \rho_3)V_o^2 z_0$ | $1/W_e$ |

The basic motions of the inner and outer interfaces are prescribed by $r_i(\tau)$ and $r_o(\tau)$, respectively, with

$$r_i(\tau)\ \dot{r}_i(\tau) = r_o(\tau)\ \dot{r}_o(\tau)$$

where the overdot indicates differentiation with respect to $\tau$. This relation is a consequence of the assumption of isochoric flow. The basic motions are then perturbed by small amounts $\eta_i Y_m Z_n$ to

$$r_1(\tau) = r_i(\tau) + \eta_1(\tau)\ Y_m Z_n \qquad \text{(inner surface)}$$

$$r_2(\tau) = r_o(\tau) + \eta_2(\tau)\ Y_m Z_n \qquad \text{(outer surface)}$$

where $Y_m = A_m \cos(m\theta) + B_m \sin(m\theta)$ , and $Z_n = \cos(n\pi z)$ .

$A_m$ and $B_m$ are constants. The index n specifies the axial mode; the index m specifies the polar (or circumferential) mode.

Analysis reveals that under the assumptions made above, we must have the same values of n and m for the two interfaces, although the magnitudes $\eta_1$ and $\eta_2$ need not be equal, and generally are not.

We find that to first order, the evolution of the disturbances $\eta_i$ is governed by the equations

$$\frac{d}{d\tau}\left(r_i f_{11}\eta_1\right) - G_1\eta_1 - r_i \frac{d}{d\tau}\left[\frac{f_{12}}{r_o}\frac{d}{d\tau}\left(r_o\eta_2\right)\right] = 0 \tag{1}$$

$$\frac{d}{d\tau}\left(r_o f_{22}\eta_2\right) - G_2\eta_2 + r_o \frac{d}{d\tau}\left[\frac{f_{21}}{r_i}\frac{d}{d\tau}\left(r_i\eta_1\right)\right] = 0 \tag{2}$$

where

$$G_1 = \left(\beta_2 - \beta_1\right)r_i\,r_i - r_i \frac{d}{d\tau}\left[\frac{\dot{r}_i}{r_i}\,f_{11}\right] + \frac{1}{r_i W_{e1}}\left[1 - m^2 - \left(kr_i\right)^2\right]$$

$$G_2 = \left(\beta_3 - \beta_2\right)r_o\,r_o - r_o \frac{d}{d\tau}\left[\frac{\dot{r}_o}{r_o}\,f_{22}\right] + \frac{1}{r_o W_{e2}}\left[1 - m^2 - \left(kr_o\right)^2\right]$$

$$f_{11} = \frac{\beta_1}{k}\frac{I_m\left(kr_i\right)}{I_m'\left(kr_i\right)} - \frac{\beta_2}{k}\frac{I_m\left(kr_i\right)K_m'\left(kr_o\right) - I_m'\left(kr_o\right)K_m\left(kr_i\right)}{I_m'\left(kr_i\right)K_m'\left(kr_o\right) - I_m'\left(kr_o\right)K_m'\left(kr_i\right)}$$

$$f_{12} = \frac{\beta_2}{k}\frac{I_m\left(kr_i\right)K_m'\left(kr_i\right) - I_m'\left(kr_i\right)K_m\left(kr_i\right)}{I_m'\left(kr_o\right)K_m'\left(kr_i\right) - I_m'\left(kr_i\right)K_m'\left(kr_o\right)}$$

$$f_{21} = \frac{\beta_2}{k}\frac{I_m\left(kr_o\right)K_m'\left(kr_o\right) - I_m'\left(kr_o\right)K_m\left(kr_o\right)}{I_m'\left(kr_i\right)K_m'\left(kr_i\right) - I_m'\left(kr_o\right)K_m'\left(kr_i\right)}$$

$$f_{22} = -\frac{\beta_3}{k}\frac{K_m(kr_o)}{K_m{}'(kr_o)} + \frac{\beta_2}{k}\frac{I_m(kr_o)\,K_m{}'(kr_i) - I_m{}'(kr_i)\,K_m(kr_o)}{I_m{}'(kr_o)\,K_m{}'(kr_i) - I_m{}'(kr_i)\,K_m{}'(kr_o)}$$

In these equations, $I_m$ is the modified Bessels function of the first kind of order m, and $K_m$ is the modified Bessels function of the second kind of order m. A prime denotes differentiation with respect to the argument.

$We_i = (\rho_1 + \rho_2 + \rho_3)V_o{}^2 z_{\emptyset}/\sigma_i$ is the Weber number of interface i.

Equations (1) and (2) resemble a Sturm-Liouville system. However, owing to the coupling between $\eta_1$ and $\eta_2$, it is not possible to assert *a priori* that the solutions are stable if the functions $G_i$ are negative, nor that the solutions are linearly unstable if the functions $G_i$ are positive. (This is because examples of such systems exist which violate this.)

Equations (1) and (2) reduce to the appropriate result for a single interface in the limit $r_i \to r_o$, and to the classical result for an infinite plane layer in the limit $r_i \to \infty$, $r_o \to \infty$, $r_i < r_o$.

Equations (1) and (2), with appropriate initial conditions, $\eta_i(0)$ and $\dot{\eta}_i(0)$, can be integrated numerically, and the behavior of the solutions determined for various values of $\beta_i$, various disturbances (m, n), and various functions $r_o(\tau)$. Cases of interest in the explosive dispersal of liquids include:

- $\beta_2 > \beta_1,\ \beta_3,$

- $\beta_1 > \beta_2 > \beta_3,$

- constant velocity expansion,

- decelerating expansion, and

- accelerating-decelerating expansion.

The behavior of the solutions to (1) and (2) for these cases is explored in Appendix 4.

We restrict our attention to (dimensional) functions $R_o(\tau)$ of the form

$$R_o(t) = R_\infty \left\{ 1 - \exp\left[ -a\left( t + t_0 \right) \right] \right\}$$

which represents a reasonable approximation, based on cloud growth data for typical fuel-air explosive clouds. $R_\infty$ is the fully expanded, equilibrium cloud radius obtained from experimental data, if available; if $R_\infty$ is unknown, $30\,R_o$ is a reasonable estimate; $a$ is a time constant obtained from experimental data, if available; otherwise a value of $0.3/\text{msec}$ represents reasonable estimate. $t_\emptyset$ is a constant, determined from

$$R_o(0) = R_\infty \left\{ 1 - \exp\left[ -a t_0 \right] \right\}$$

In dimensionless variables,

$$r_o(\tau) = r_\infty \left\{ 1 - \exp\left[ -a^*\left( \tau + \tau_0 \right) \right] \right\}$$

where $a^* = z_\emptyset / R_\infty$ and $r_\infty = R_\infty / z_\emptyset$. A convenient velocity scale is then $V_o = a R_\infty$.

Examination of typical values for $\beta_i$ and typical expressions for $r_o(\tau)$ show that, in the absence of surface tension (see Appendix 4)

- Radially expanding films are inherently unstable: there always exist modes which are amplified, even for a constant velocity expansion.

- The instability may be oscillatory: the amplitudes behave like $\exp(\lambda t)$, where $\text{Im}\{\lambda\} \neq 0$.

- Disturbances with smaller values of n and m tend to be more unstable than those with larger values.

Adding surface tension tends to stabilize the films, but does not eliminate the instability.

To use the model, we can estimate the breakup time and initial drop diameter from the time when the amplitude of the instabilities equals the thickness of the film, for some appropriate initial conditions $\eta_i(0)$ and $\dot{\eta}_i(0)$, i.e., the breakup time $\tau_b$ is the time when

- 24 -

$$\max\left\{\left|\eta_1\left(\tau_b\right)\right| \ , \ \left|\eta_2\left(\tau_b\right)\right|\right\} = r_o\left(\tau_b\right) - r_i\left(\tau_b\right) = w\left(\tau_b\right)$$

where $w(\tau)$ is the dimensionless film thickness, and the initial drop diameter is estimated to be

$$d \leq 2w\left(\tau_b\right) \quad ,$$

where $d$ is the dimensionless drop diameter. The dimensional drop diameter, $D(t)$, is $d(\tau)z_\emptyset$, and the dimensional film thickness $W(t)$ is $w(\tau)z_\emptyset$.

The linear stability model is valid only for $\left|\eta_i(\tau)\right|$ very much less than one. To predict the breakup time and the initial average drop diameter, it is necessary to violate this criterion; *i.e.*, to use the linear model in a flow regime where a nonlinear model is required for accurate predictions. This means that the predicted breakup time will be too small, and the predicted initial arithmetic average drop diameter will be too large.

The predicted breakup time is too small because the growth rate of these instabilities is known to decrease in the nonlinear regime [21]. Consequently, the estimates of the breakup time made with the linear film instability model will underestimate the breakup time.

The predicted initial arithmetic average drop diameter will be too large because in the nonlinear regime the small-scale components of the evolving disturbance grow faster than the large-scale ones [21]. Thus the disturbance modes that cause the breakup will be smaller (*i.e.*, will have larger values of n and/or m) than the critical ones indicated by the linear film instability model. Hence the breakup will produce smaller initial arithmetic average drop diameters than those indicated by the linear film instability model.

However, the model can be used to place a lower bound on the breakup time and an upper bound on the initial drop diameter. In the absence of more precise data, these bounds provide useful information for parameter studies with the far-field dispersal model.

In addition, since the initial conditions are unknown, we can take the largest permissible values of $\left|\eta_i(0)\right|$ and $\left|\dot{\eta}_i(0)\right|$ to produce the fastest growing disturbances (in the linear model) and hence the earliest

- 25 -

estimated breakup time and the largest estimated initial arithmetic average drop diameter.

The initial conditions used for integrating (1) and (2) were $\eta_1(0) = -0.01$, $\eta_2(0) = \dot{\eta}_1(0) = \dot{\eta}_2(0) = 0$. The evolution of $\eta_i$ and $w(\tau)$ is shown in Figure 9. Numerical results are given in Table 2. The experimental device used by Samirant et al. was a cylindrical annulus with an inner radius of 1.5 cm, an outer radius of 5.5 cm, and a height of 12 cm, containing ethylene oxide.

Table 2: Comparison of the breakup time and drop diameter predicted by the film instability model with the experimental results of Samirant et al. for ethylene oxide.

| Source | Breakup Time [msec] | Arithmetic Average Drop Diameter [cm] |
|---|---|---|
| Samirant et al.[12] | 1.3 | 0.5 |
| Film Instability | 0.11 | 0.44 |

* For the film instability model, the drop diameter at breakup was computed from $d = w(\tau_b)$.

As expected, the estimated breakup time is less than the measured breakup time. The estimated initial arithmetic average drop diameter is slightly less than the measured drop diameter. However, according to Samirant *et al.* [12], immediately prior to breakup the film thickness was 3 mm, and immediately after breakup the arithmetic average drop diameter was 5 mm. The film instability model predicts a film thickness and an arithmetic average drop diameter at breakup of 4.4 cm. This suggests that the linear model slightly over-estimates the film thickness at breakup, and that the initial arithmetic average drop diameter is between one and two times the film thickness just prior to breakup.
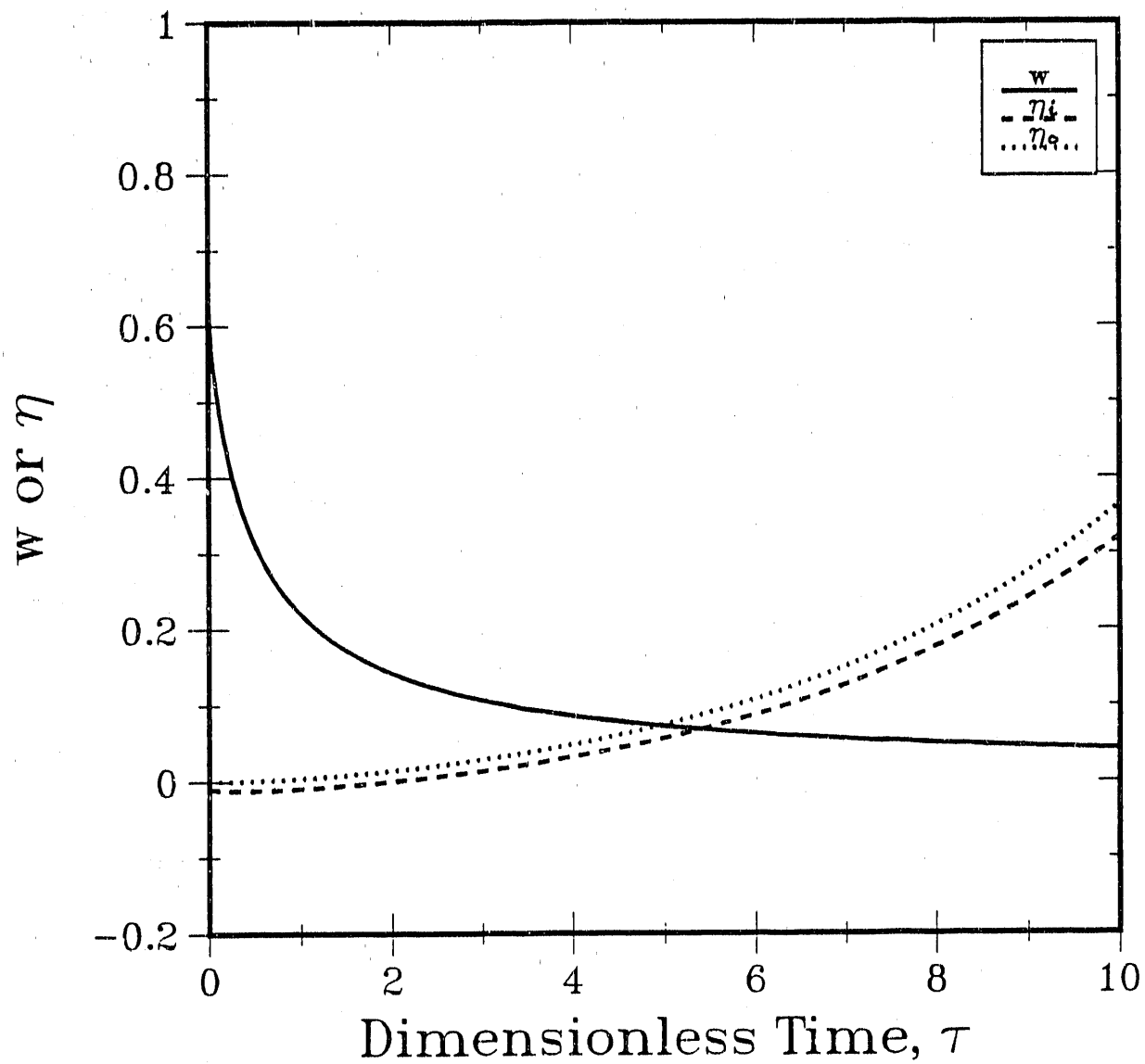
Figure 9: Evolution of the disturbances $\eta_i$ and the film thickness $w(\tau)$.

## 3.2 Summary of the Film Instability Model

The film instability model places a

- lower bound on the breakup time, and

- lower bound and an upper bound on the initial
  arithmetic average drop diameter.

To use the model, we estimate the breakup time and initial drop diameter from the time when the amplitude of the fastest growing instability (obtained by integrating (1) and (2) numerically) equals the thickness of the film, for initial conditions $\eta_i(0)$ and $\dot{\eta}_i(0)$ given by

$$|\eta_i(0)| = \max\{\min\{0.01, \ (1.0 \text{ mm})/z_{\emptyset}\}, \ 0.01\}$$

and

$$|\dot{\eta}_i(0)| = \max\{\min\{0.01, \ (1.0 \text{ m/sec})/(\alpha R_{\infty})\}, \ 0.01\}$$

where $\alpha R_{\infty}$ is the velocity scale.

The dimensionless breakup time $\tau_b$ is the time when

$$\max\{|\eta_1(\tau_b)|, \ |\eta_2(\tau_b)|\} = r_o(\tau_b) - r_i(\tau_b) = w(\tau_b),$$

where $w(\tau)$ is the dimensionless film thickness, and the initial average dimensionless drop diameter d is

$$w(\tau_b) \leq d \leq 2 \ w(\tau_b).$$

## 4.  THE COMBINED NEAR-FIELD DISPERSAL MODEL

The final near-field dispersal model is a combination of the CTH hydro-dynamics code and the film instability model.

CTH provides predictions of the temperature, pressure, and velocity fields, and the bulk material distribution.

Lower and upper bounds on the initial arithmetic average drop diameter are obtained from the film stability model, which was described in Section 3.

This information is provided to the far-field model as a CTH restart file (at a time after the predicted breakup time), and a prediction of the initial arithmetic average drop diameter.

Results from the simulation of a typical near-field dispersal are shown in Figures 3-7 for the initial device shown in Figure 2. The CTH input files and run history milestones for this simulation are given in Appendix 1.

The breakup time and initial arithmetic average drop diameter at breakup predicted for this simulation by the film stability model are

$$t_b = 0.45 \text{ msec and } 1.4 \text{ cm} \leq D_b \leq 2.8 \text{ cm}.$$

These were calculated with $\eta_1 = \dot{\eta}_1 = -0.01$, $\eta_2 = \dot{\eta}_2 = 0.01$, and no sur-face tension. Surface tension was ignored at the inner interface because the high temperature of the inner interface (Figure 5) indicates that the surface tension is very small there. The estimated Weber number for the outer interface is on the order of $8 \times 10^9$; from the definition of the function $G_2$ (following equation 2), this large Weber number introduces a negligible influence on the evolution of $\eta_i$.

The continuation of a near-field simulation into the far-field is described in another report [22].

# 5. CONCLUSIONS AND RECOMMENDATIONS

A model has been described for predicting the conditions in the early phases of the formation and expansion of a fuel-air cloud, for liquid fuels. In the archetypical fuel-air device, the liquid fuel is contained in a canister in the form of a cylindrical annulus. The central cylinder contains the high explosive burster charge.

The model consists of the CTH hydrodynamics code and an analytical model, the film instability model. CTH provides predictions of the temperature, pressure, and velocity fields and the bulk material distribution. The film instability model provides a lower bound on the time at which the bulk liquid breaks up into drops and upper and lower bounds on the initial arithmetic average diameters of the drops.

The model is valid in the near-field regime, where explosive forces dominate or are approximately equal in magnitude to the aerodynamic drag forces acting on the drops. Predictions of near-field cloud behavior and initial arithmetic average drop diameter by the model compare favorably with the behavior and diameter shown in high-speed movies of typical fuel dispersal experiments. However, the model remains largely untested against experimental data owing to the sparsity of such data.

The model is to be used to provide initial conditions for the far-field model, KIVA-FAE [23], which is valid in the regime where aerodynamic forces on the fuel drops dominate the explosive forces.

The near-field dispersal model ignores the effects of the canister fragments on the breakup process and the flow field. The fragments may induce turbulence in the expanding cloud; such turbulence would improve the comminution of the fuel and the air, producing a more uniform fuel distribution in the cloud. The fragments may also influence the liquid breakup, since at very early times the liquid squirts through the gaps between the fragments.

The near-field model is inapplicable to solid fuels; an entirely different near-field model will be required to simulate the dispersal of solid fuel particles. The degree to which solid fuels are compacted, agglomerate, and shatter is unknown. Simulations of explosive dispersal of a loosely packed powder (0.5 void fraction) and high fuel-to-burster mass ratios (35:1) [24] indicate that significant compaction of the solid particulate powders occurs. In contrast, in real fuel-air explosive devices the solid fuel powders will be compacted to high

densities when the fuel canisters are loaded, and the fuel-to-burster mass ratios will be higher, on the order of 100:1. The effects of these differences on the particle sizes and particle size distributions in the fuel-air cloud are unknown.

The near-field dispersal model provides a reasonable set of initial conditions for the far-field dispersal model. Validation of the model must await the availability of experimental data in the near field regime of a fuel-air explosive cloud. This model is the first to address the behavior of expanding liquid fuel in the near-field regime, and in particular, it is the first model to address the breakup of liquid fuels into drops.

**APPENDIX 1:    CTH Input for the Simulation of the Dispersal of Decane into Air**

The input files and run history for the CTH simulation of the dispersal of liquid decane into air by detonation of a central burster charge of PBX9010 (Figures 2-7) are presented in this appendix. The files are presented for reference only; no attempt will be made to explain all the entries in these files. The interested reader is referred to the latest version of the CTH User's Guide ([15]; contact the authors) for explanation of the structure of the files and the significance of the entries.

CTH consists of a preprocessor called CTHGEN, the main computational module called CTH, and a file post-processor called CTHED, and a graphics post-processor called CTHPLT.

CTHGEN establishes a restart file for CTH. The CTHGEN input file specifies the computational grid, and specifies the materials and their location in the grid. In the cthgen input file, all characters to the right of an asterisk are ignored. Both CTHGEN and CTH use the ANEOS analytical equation of state models [15].

CTH performs advances the simulation in time, starting with the system state specified in the restart file. As in the cthgen input file, all characters to the right of an asterisk in the cth input file are ignored.

CTHED is an interactive program that used to examine data encoded in the restart file, to edit the restart file, and to create files from which various one-, two-, and three-dimensional plots can be made with CTHPLT.

Milestones in the run history for the simulation of the dispersal of liquid decane into air were:

- The computational grid shown in Figure 2 was used from a problem time of 0 msec to a time of 0.25 msec.

- At 0.25 msec, the problem was rezoned to a uniform grid with computational cells 1 cm in the radial direction and 1 cm in the axial direction. The small aluminum plug was removed during the rezoning, as it was no longer influencing the flow significantly.

- Following the rezoning, the simulation was extended to a time of 2 msec.

Total cpu time required for the simulation was on the order of 52 cpu minutes.

```
**********************************************************************
*
*                            cthgen input
*
*--------+---------+---------+---------+---------+---------+---------+
*
*   Simulation 16e -- Coarse Mesh.
*
*   This is a test FAE problem to track fuel concentration as a func-
*   tion of time for a 'typical' NWC jug FAE device.  The device is
*   an idealization of an Arrowhead purified water bottle.  The water
*   bottle itself is ignored, as is the glass tube containing the HE
*   burster charge.  The fuel is decane, and the burster charge is
*   PBX9010 (90% RDX, 10% Kel-F).  The Aneos input values for decane
*   were devised by D. R. Gardner; the PBX9010 Aneos input values are
*   the appropriate JWL parameter values.  The aluminum plug atop the
*   burster charge is modeled using a library equation of state.
*
*   The PBX9010 explosive is detonated as a line charge, which extends
*   from z=0 to z=12.70 cm.  The charge is 0.98032 cm in radius.  The
*   outer radius of the decane is 13 cm.  The half-height of the device
*   is 17.78 cm (7 inches).  The simulation is axisymmetric, and by
*   virtue of symmetry, only one half of the axial length is modeled.
*
*
*
*            z
*
*                        Air                          Air
*
*            |
*            |
*           |Al|  _____
*            |  |                           |
*            |  |                           |
*            |  |                           |
*            | --                           |
*            |P |                           |
*            |B |                           |
*            |X |      Decane               |            Air
*            |9 |                           |
*            |0 |                           |
*            |1 |                           |
*            |0 |                           |
*            |  |                           |
*            |  |                           |
*            |__|_____|__       r
*
*
*--------+---------+---------+---------+---------+---------+---------+
*
*  Title
*
CTH Simulation 16d: Decane dispersed by PBX9010
```

- 34 -

```
*
*---------+---------+---------+---------+---------+---------+---------+
*
CONTROL
 *  BGTEMPERATURE = 0.02567785 * Background temperature for voids.
    MMT                        * Give each material its own temperature.
 *  TIME = 0.0                 * Problem start time.
 *  VISCOSITY  BL=0.1  BQ = 2. * Artificial viscosity coefficients.
ENDCONTROL
*
EDIT
   Block = 1
     Noexpanded
   Endblock
ENDEDIT
*
*
*---------+---------+---------+---------+---------+---------+---------+
*
MESH
*
   Block 1    Geometry = 2DCylindrical  Type = Eulerian
*
   x0 = 0.0
      x1  Number_of_cells =    5   Width =   1.0    Ratio = 1.0
      x2  Width =  19.0    DXFirst = 0.2    DXLast = 1.0
      x3  Number_of_cells = 80   Width =  80.0    Ratio = 1.0
   Endx
*
   y0 = 0.0
      y1  Number_of_cells = 100   Width = 100.0   Ratio = 1.0
   Endy
*
*  Activate small portion of mesh.
*
   Xaction = 0.0,  5.0
   Yaction = 0.0, 15.0
*
   Endblock
*
ENDMESH
*
*---------+---------+---------+---------+---------+---------+---------+
*
Insertion_of_Material
*
   Block 1
*
*
```

```
  Package  = PBX9010
  Material = 3
  Density  = 1.787
  Numsub   = 10
  Pressure = 1.01325E+6
*
    Insert Box
    x1 =  0.00    x2 =  0.98032
    y1 =  0.00    y2 = 12.70
    Endinsert
*
  Endpackage
*
*
  Package  = 'Aluminum Plug'
  Material = 4
  Pressure = 1.01325E+6
*
    Insert Box
    x1 =  0.00    x2 = 0.98032
    y1 =  0.00    y2 = 17.78
    Endinsert
*
  Endpackage
*
*
  Package  = 'Decane'
  Material = 2
  Density  = 0.7263
  Pressure = 1.01325E+6
*
    Insert Box
    x1 =  0.00    x2 = 13.00
    y1 =  0.00    y2 = 17.78
    Endinsert
*
  Endpackage
*
*
  Package  = 'Dry Air'
  Material = 1
  Pressure = 1.01325E+6
*
    Insert Box
    x1 =  0.00    x2 = 100.0
    y1 =  0.00    y2 = 100.0
    Endinsert
*
  Endpackage
*
*
```

```
     Endblock
*
Endinsertion
*
*---------+----------+----------+----------+----------+----------+----------+
*
* Equation of State Informatioı.
*
EOS Number_of_materials = 4
*
  Material1 = -1              * Dry Air
  Material2 = -2              * Decane
  Material3 = -3              * PBX9010
  Material4 = -4              * Aluminum
*
*
aneos0 -1 'Dry Air'
aneos1  3.0 -2.0  1.1830E-3   0.0  0.0  0.0  0.400  0.000
aneos2  0    0.0  8.33924E10  0.0  0.0  0 0  0        0
aneos3  0.0  0.0  0.000       0.0  0.0  0    0        0
aneos4  7.0  0.7809
aneos5  8.0  0.2095
aneos6 18.0  0.0096
*
*ANEOS inputs for decane were compiled by D. R. Gardner (6425).
aneos0 -2 'Decane'
aneos1  2.0   3.0   0.7700   0.02097742   1.01325E6    1.500E10    0.300
0.000
aneos2  0     2.0   9.42E10  0.02097742   0.0000       0.0    0    0
aneos3  0.5   0.0   0.000    0.00         0.000        0      0    0
aneos4  1.0   22.0
aneos5  6.0   10.0
*
*ANEOS inputs for pbx9010 were compiled by D. R. Gardner (6425).
aneos0 -3 'PBX9010'
aneos1   6.0   -3.0      1.7870    0.02567785   1.01325E6 1.0   0.350   0.0
aneos2   0.0    0.0      0.000     0.0411       0.0000    0.0   0       0
aneos3   0.0    5.814    0.06801   4.10         1.00      0     0       0
aneos4   1      0.2694
aneos5   6      0.1537
aneos6   7      0.2694
aneos7   8      0.2694
aneos8   9      0.0258
aneos9  17      0.0095
*
aneos0 -4 'Aluminum'  LIB = 3   TYPE = 0
*
ENDEUS
*
*
```

```
HEBURN
*
  Material = 3                               &
  Detonation_Velocity = 8.500E+5             &
  Rho = 1.787                                &
  Temperature = 0.02567785                   &
  Number_of_cells_in_burn_front = 2          &
  Predetonation_Pressure = 5.0E+15
*
  Dline = 0.0, 0.0 to 0.0, 12.70             &
      Radius = 0.98032                       &
      Time   = 0.0
*
ENDHEBURN
*
*
TRACER
*  Add Lagrangian tracer particles.
*
*     On each side of the PBX9010-decane interface:
   ADD   0.90, 2.0   TO   0.90, 10.0   NUMBER 5
   ADD   1.10, 2.0   TU   1.10, 10.0   NUMBER 5
*
*     On the decane side of the decane-air interface:
   ADD   12.5, 2.0   TO 12.50, 10.0   NUMBER 5
*
ENDTRACER
*
ENDINPUT                        * End of cthgen input
*
*---------+---------+---------+---------+---------+---------+---------+
```

```
*********************************************************************************
*
*                                  cth input
*
*----------+----------+----------+----------+----------+----------+----------+
*
*   Simulation 16d -- Coarse Mesh.
*
*   This is a test FAE problem to track fuel concentration as a func-
*   tion of time for a 'typical' NWC jug FAE device.  The device is
*   an idealization of an Arrowhead purified water bottle.  The water
*   bottle itself is ignored, as is the glass tube containing the HE
*   burster charge.  The fuel is decane, and the burster charge is
*   PBX9010 (90% RDX, 10% Kel-F).  The Aneos input values for decane
*   were devised by D. R. Gardner; the PBX9010 Aneos input values are
*   the appropriate JWL parameter values.  The aluminum plug atop the
*   burster charge is modeled using a library equation of state.
*
*   The PBX9010 explosive is detonated as a line charge, which extends
*   from z=0 to z=12.70 cm.  The charge is 0.98032 cm in radius.  The
*   outer radius of the decane is 13 cm.  The half-height of the device
*   is 17.78 cm (7 inches).  The simulation is axisymmetric, and by
*   virtue of symmetry, only one half of the axial length is modeled.
*
*
*
*             z
*                            Air                          Air
*
*             |
*             |
*             | _____
*           |Al|                                        |
*             |  |                                        |
*             |  |                                        |
*             | --|                                        |
*             |P |                                        |
*             |B |                                        |
*             |X |           Decane                      |           Air
*             |9 |                                        |
*             |0 |                                        |
*             |1 |                                        |
*             |0 |                                        |
*             |  |                                        |
*             |  |                                        |
*             |__|_____|____ r
*
*----------+----------+----------+----------+----------+----------+----------+
*
*   Title
*
```

- 39 -

CTH Simulation 16d: Decane dispersed by PBX9010
*
*---------+---------+---------+---------+---------+---------+---------+
*
CONTROL
* BIGedit
* CPShift
* DTCourant = <.6>
* DTFfrac = <1.>
* DTIncrease = <1.068000433>
* DTStart
* ELEDIT
* GRAVity = <0.>
  NLEdit
  NLFedit
  NTBad   = 10000
* NSCycle = <55000>
  PVOid = 1.01325E6
  RDUmpf = 3600.
  TSTop = 1.e-4
* USEssd
* VIScosity  BL=<0.1>  BQ = <2.>
ENDC
*
*---------+---------+---------+---------+---------+---------+---------+
*
CONVCT
  CONVECTION = 0.
  Interface  = High_Resolution
ENDC
*
*---------+---------+---------+---------+---------+---------+---------+
*
BOUNDARY
  BHYDRO
    BLock = 1
    BXBot = 0
    BXTop = 1
    BYBot = 0
    BYTop = 1
    ENDB
  ENDH
ENDB
*---------+---------+---------+---------+---------+---------+---------+
*
EDIT
  SHORTT
    TIME = 0.       DTFrequency = 1.0e-7
    TIME = 1.0e-6  DTFrequency = 1.0e-6
    TIME = 1.0e-5  DTFrequency = 1.0e-5
    TIME = 1.0e-4  DTFrequency = 1.0e-4
    TIME = 1.0e-3  DTFrequency = 1.0e-3
  ENDS

```
*
  LONGT
    TIME = 0.        DTFrequency = 1.0E-3
  ENDL
*
  PLOTT
    TIME = 0.        DTFrequency = 1.0e-7
    TIME = 1.0e-6    DTFrequency = 1.0e-6
    TIME = 1.0e-5    DTFrequency = 1.0e-5
    TIME = 1.0e-4    DTFrequency = 1.0e-4
    TIME = 1.0e-3    DTFrequency = 1.0e-3
  ENDP
*
  HISTT
    TIME = 0.        DTFrequency = 1.0e-6
    TIME = 1.0e-5    DTFrequency = 1.0e-5
    TIME = 1.0e-4    DTFrequency = 1.0e-4
    TIME = 1.0e-3    DTFrequency = 1.0e-3
*
  HTRACER1
  HTRACER2
  HTRACER3
  HTRACER4
  HTRACER5
  HTRACER6
  HTRACER7
  HTRACER8
  HTRACER9
  HTRACER10
  HTRACER11
  HTRACER12
  HTRACER13
  HTRACER14
  HTRACER15
  ENDH
*
*
ENDE
*
*                                End of CTH input
*
*---------+---------+---------+---------+---------+---------+---------+
```

# APPENDIX 2:  A Surface Tension Model

Consider a cylindrical annulus of fluid.  The fluid is assumed to be incompressible.  The length of the annulus is $2z_\emptyset$; its inner radius is $R_i(t)$ and its outer radius is $R_o(t)$.  The surface tension at the inner and outer surfaces is $\sigma$.  We assume that the fluid is moving radially only, and that the flow is isothermal.  The free energy of the surfaces is

$$E_s = 2\pi z_\emptyset \sigma [R_i(t) + R_o(t)].$$

Suppose that the film breaks up into a monodisperse field of drops with diameter d.  If the total volume of the liquid is V, then the number of drops N and the total surface area of the drops $A_d$ is

$$N = 6V/(\pi d^3), \quad \text{and} \quad A_d = N_d \pi d^2 = 6V/d.$$

The total free energy of the drop surfaces is

$$E_d = \sigma A_d = 6\sigma V/d.$$

The total volume of fluid is $V = 2z_\emptyset \pi [R_o^2(0) - R_i^2(0)]$.

Initially, and for some $0 < t < t_b$, the free energy of the annular surfaces is less than the free energy of that same fluid if it existed as drops of diameter d:  $E_s < E_d$.  As the fluid expands, it reaches a state where the two free energies are equal:  $E_s = E_d$.  At later times the free energy of the annular surfaces is greater than the free energy of that same liquid if it existed as drops of diameter d:  $E_s > E_d$.  At these later times, it is energetically more favorable for the fluid to exist as drops, rather than as a film.  We assume then that breakup of the film into drops occurs when the two free energies are equal:  $E_s = E_d$.

We can thus define a parameter $E_{sd} = E_d/E_s$ such that breakup occurs when $E_{sd} = 1$.  This leads to the expression:

$$\frac{E_s}{E_d} = \frac{\beta d[r_o(\tau) + r_i(\tau)]}{1 - (R_i/R_o)^2} = 1 \tag{2.1}$$

where $r_i(\tau) = R_i(t)/z_\emptyset$, $r_o(\tau) = R_o(t)/z_\emptyset$, $\tau = t/T_\emptyset$, $R_i = R_i(0)$, $R_o = R_o(0)$, $d = d/z_\emptyset$, and $\beta = (z_\emptyset/R_o)^2/3$.  $T_\emptyset$ is a time scale.

Equation (2.1) can be solved for d:

$$d = \frac{1}{\beta} \frac{1 - (R_i/R_o)^2}{r_o(\tau) + r_i(\tau)} \qquad (2.2)$$

Equation (2.2) can be evaluated if expressions are known for $r_i(\tau)$ and $r_o(\tau)$.

Assuming that the fluid is incompressible and moves only in the radial direction allows us to write

$$2\pi z_\emptyset [R_o^2(t) - R_i^2(t)] = 2\pi z_\emptyset [R_o^2(0) - R_i^2(0)]$$

and hence $R_o(t)U_o(t) = R_i(t)U_i(t)$, where U is the velocity. Then assuming that $R_o(t)$ has the form

$$R_o(t) = R_\infty\{ 1 - \exp[-\alpha(t + t_\emptyset)]\} \qquad (2.3)$$

we can derive expressions for $r_o(\tau)$ and $r_i(\tau)$. Equation (2.3) represents a reasonable approximation, based on cloud growth data for typical fuel-air explosive clouds. $R_\infty$ is the fully-expanded, equilibrium cloud radius, $\alpha$ is a time constant, and $t_\emptyset$ is determined from

$$R_o(0) = R_\infty\{ 1 - \exp[-\alpha t_\emptyset]\}$$

From (2.3) we can construct a time scale using $\alpha R_\infty$ and $z_\emptyset$: $T_\emptyset = z_\emptyset/(\alpha R_\infty)$. Then

$$r_o(\tau) = r_\infty\{ 1 - \exp[-\alpha^*(\tau + \tau_\emptyset)]\} \qquad (2.4)$$

where $\alpha_* = z_\emptyset/R_\infty$ and $r_\infty = R_\infty/z_\emptyset$.

Equations (2.2) and (2.4) provide an estimate of the initial drop diameter at breakup, if the breakup time is known. Conversely, if the initial drop diameter is known, then the breakup time can be estimated.

Predictions from the model can be compared to the measured breakup time and initial drop diameter reported by Samirant et al. [12] for a device in which $z_\emptyset = 6.0$ cm, $R_o(0) = 5.5$ cm, and $R_i(0) = 1.5$ cm. Using the velocity data presented in [12], $R_\infty = 184.10$ cm, $t_\emptyset = 0.020641$ msec, and $\alpha = 1.4695$/msec; thus $\alpha^* = 0.032591$, $r_\infty = 30.683$, $\tau_\emptyset = 0.93069$, and

$$r_o(\tau) = 30.683 \{ 1 - \exp[-0.032591(\tau + 0.93069)]\}$$

Predictions for the initial arithmetic average drop diameter as a function of breakup time for this model device are given in Figure 10.

Predictions of the breakup time as a function of the initial arithmetic average drop diameter for this model device are given in Figure 11.

Predictions of the initial arithmetic average drop diameter and breakup time are given in Table 3, and compared with the measured values of Samirant et al. [12].

The predicted breakup time (when the initial drop diameter is known) is too small by a factor of three. The predicted initial drop diameter (when the liquid breakup time is known) is too small by a factor of two. The predicted values are of the correct order of magnitude, but do not provide very accurate predictions of the liquid breakup time and the initial drop diameter. However, considering the assumptions made in the model, this agreement is quite good.

Since either the breakup time or the initial arithmetic average drop diameter at breakup must be known to use this model, and since in general neither of these quantities is known, this model is not especially useful in dispersal modeling for fuel-air explosives.

Table 3: The surface tension model predicts breakup quantities that compare favorably with the experimental results.

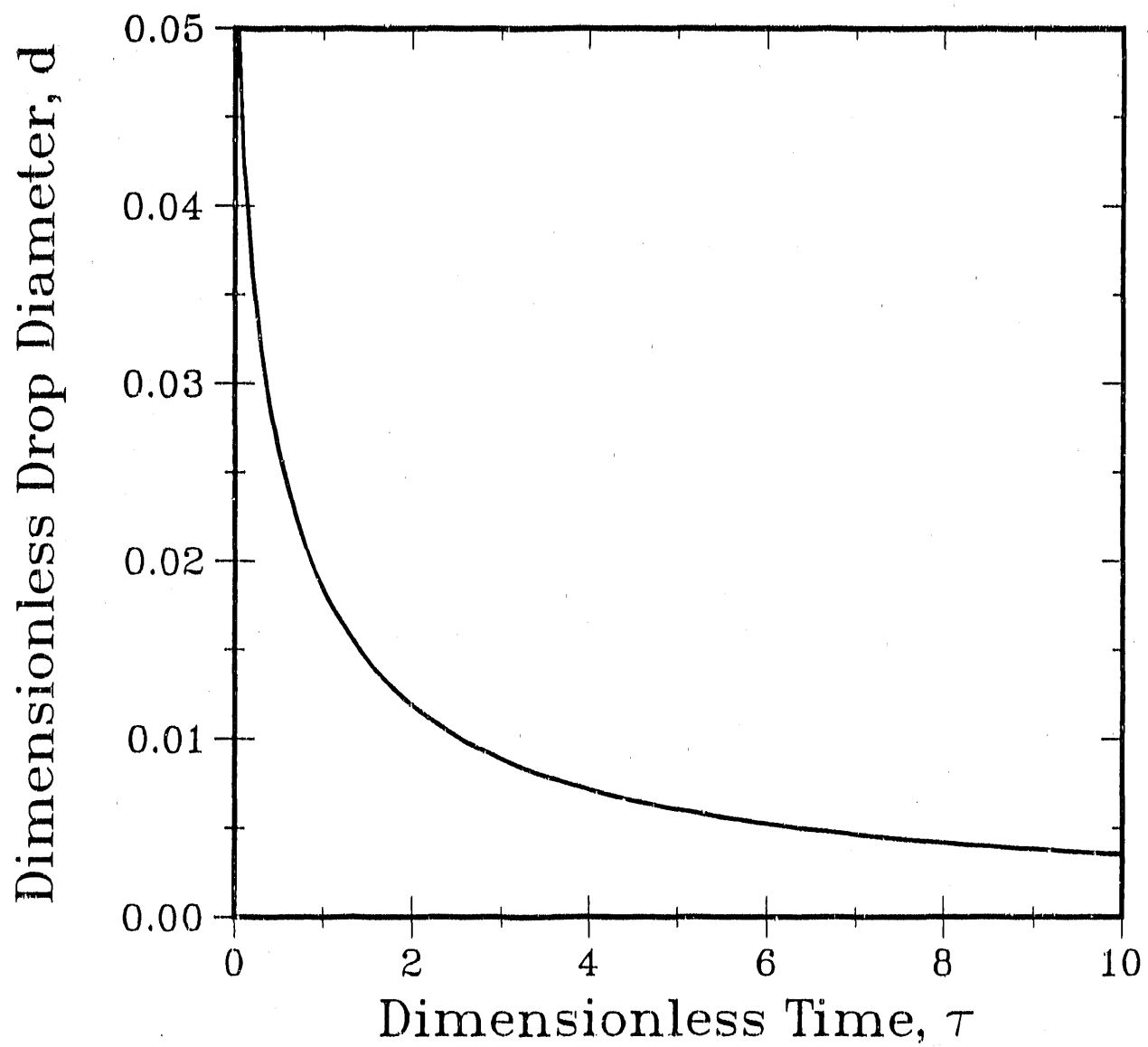| Source | Breakup Time [msec] | Arithmetic Average Drop Diameter [cm] |
|---|---|---|
| Samirant et al. [12] | 1.3 | 0.5 |
| Surface tension (assuming drop dia- meter of 0.5 cm) | 0.39 | --- |
| Surface tension (assuming breakup time of 1.3 msec) | ---- | 0.27 |

Figure 10: The initial arithmetic average drop diameter predicted by the surface tension model, as a function of the breakup time.
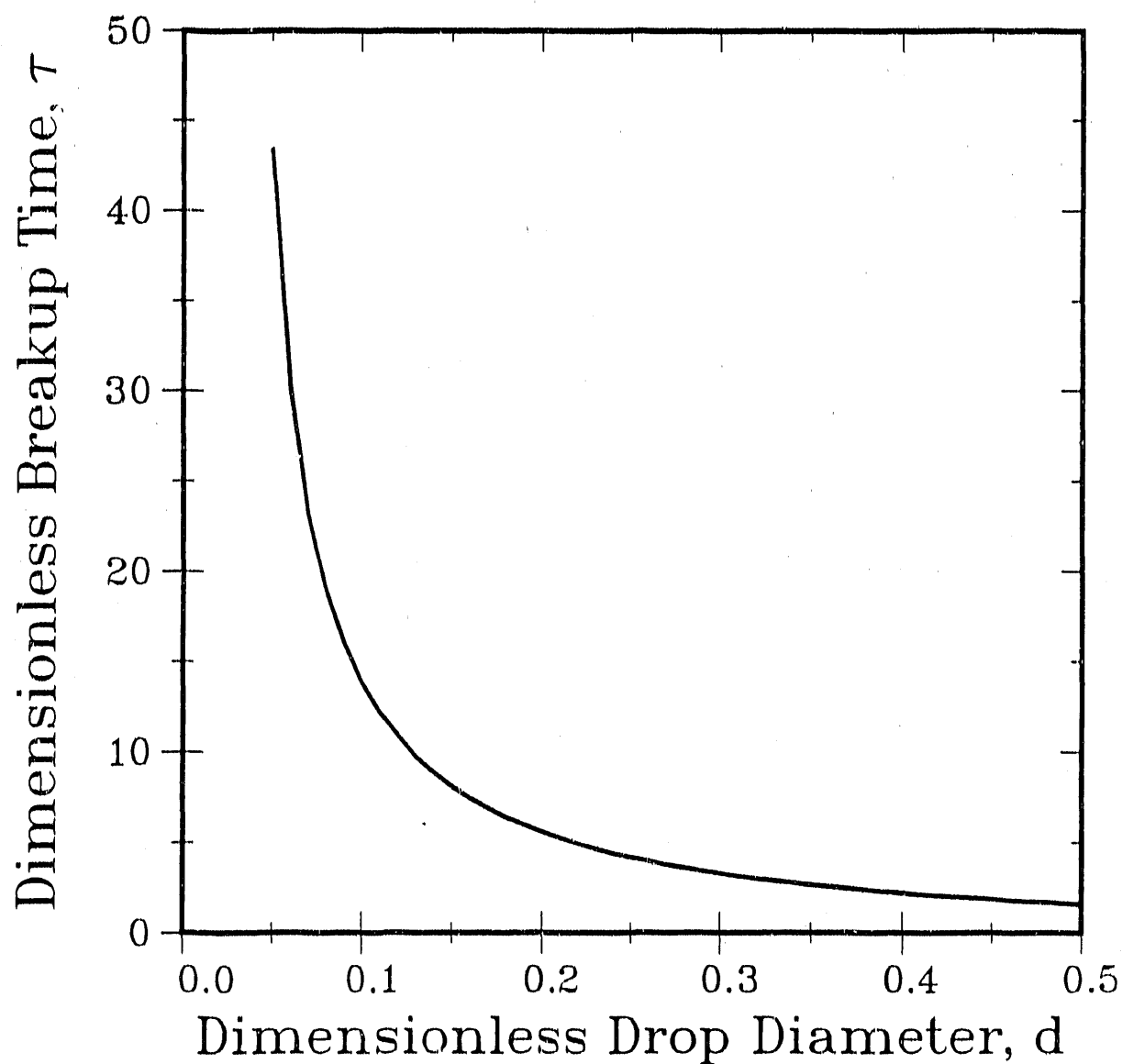
Figure 11: The breakup time predicted by the surface tension model, as a function of the initial arithmetic average drop diameter.

## APPENDIX 3:  The Grady Fracture Model

The Grady fracture model was developed by D. E. Grady (1534) for esti-
mating fragment sizes in the explosive fracture of solids.  It has been
used successfully to estimate the sizes of fragments produced in the
brittle fracture of oil shale and steel [16], the explosive loading of
cylindrical shells of uranium [17], the impact fragmentation of lead and
uranium plates [18], and the brittle and ductile spall of a variety of
metals [19].

The assumptions underlying the Grady model do not limit it *a priori* to
solids.  However, comparison with the limited data available for liquid
spall suggest that is not as useful as the models presented in Section 3
for estimating the breakup time and initial drop diameter for
explosively dispersed liquids.

The Grady model is described here briefly, and some predictions are made
with it for comparison with the data of Samirant *et al.* [12].  The
predictions of the Grady model do not match this data as well as the
predictions given in Section 3.

## The Grady Fracture Model

As applied to liquids [19], the Grady fracture model takes the following
form for energy-limited spall (see also Table 4):

For spall dominated by surface tension:

$$P_b = \left( 2\rho\ C_o^2\ \mu\dot{\epsilon} \right)^{1/2} \ , \qquad t_b = \frac{1}{C_o} \left[ \frac{6\sigma}{\rho\dot{\epsilon}^2} \right]^{1/3} \ , \quad \text{and } D_b = \left( \frac{48\sigma}{\rho\dot{\epsilon}^2} \right)^{1/3} \ .$$

For spall dominated by viscous dissipation:

$$P_b = \left( 2\rho\ C_o^2\ \mu\dot{\epsilon} \right)^{1/2} \ , \quad t_b = \left( 2\mu/\rho c_o^2\ \dot{\epsilon} \right)^{1/2} \ , \quad \text{and } D_b = (8\mu/\rho\dot{\epsilon})^{1/2} \ .$$

In these equations, $P_b$ is the spall strength of the liquid, and $t_b$ is
the time at which the liquid breaks into ''fragments'' of size $D_b$.  $\sigma$ is
the liquid surface tension, $\rho$ is the liquid density, $C_o$ is the speed of
sound in the liquid, $\mu$ is the dynamic viscosity of the liquid, and $\dot{\epsilon}$ is
the strain rate.

Using the previous approximation for the location of the outer boundary of the expanding liquid shell, we have

$$\dot{\epsilon} = (\sqrt{2}/a)\{\exp[-a(t+t_o)] - 1\}.$$

The breakup time and initial arithmetic average drop diameter predicted by the Grady fracture model for the device used by Samirant et al. [12], using the values of the material properties for ethylene oxide shown in Table 5 (in the absence of a known value, $c_o$ has been approximated using a value typical for similar liquids) are given in Table 6. Included are predictions for spall dominated by surface tension or by viscous dissipation.

For either extreme, the breakup time and initial arithmetic average drop diameter predicted by the Grady model are both far too small, compared to the experimental data. This is probably because in the explosive dispersal of liquids, spalling is not the dominant mode of liquid breakup [1, 20].

Table 4: The equations for the Grady fracture model.

| Parameter | Surface Tension Dominated Spall | Viscous Dissipation Dominated Spall |
|---|---|---|
| Breakup Time $t_b$ | $\dfrac{1}{C_o}\left[\dfrac{6\sigma}{\rho\dot{\epsilon}^2}\right]^{1/3}$ | $\left(2\mu/\rho C_o^2\dot{\epsilon}\right)^{1/2}$ |
| Drop Diameter, $D_b$ | $\left[\dfrac{48\sigma}{\rho\dot{\epsilon}^2}\right]^{1/3}$ | $(8\mu/\rho\dot{\epsilon})^{1/2}$ |
| Spall Strength, $P_b$ | $\left(6\rho^2 C_o^3 \sigma\dot{\epsilon}\right)^{1/3}$ | $\left(2\rho C_o^2 \mu\dot{\epsilon}\right)^{1/2}$ <br> --- |

Table 5:  Ethylene oxide property values.

| | |
|---|---|
| Density, kg/m$^3$ | 899 |
| Surface Tension, N/m | $2.42 \times 10^{-2}$ |
| Dynamic Viscosity, kg/m-s | $3.1 \times 10^{-3}$ |
| Sound Speed, m/s (estimated from similar liquids) | $\sim 1.6 \times 10^3$ |

Table 6:  Breakup time and initial arithmetic average drop diameter predicted by the Grady Fracture Model.

| Parameter | Breakup Time, $t_b$ [msec] | Initial Average Drop Diameter, $d_b$ [cm] |
|---|---|---|
| Surface Tension Dominated | $2.1 \times 10^{-5}$ | $6.6 \times 10^{-3}$ |
| Viscous Dissipation Dominated | $2.1 \times 10^{-6}$ | $6.7 \times 10^{-4}$ |
| Data from Samirant et al. [12] | 1.3 | 0.5 |

## APPENDIX 4: Development of the Film Instability Model

Presented in this appendix are some details of the development of the film instability model (Section 3), and the parametric study of the model for cases of interest in fuel-air dispersal studies.

Consider a cylinder of fluid, denoted fluid 1, of radius $R_i(t)$, where t represents time, and height $2z_\emptyset$. This is surrounded by an annulus of fluid, denoted fluid 2, of outer radius $R_o(t)$ and also of height $2z_\emptyset$. Surrounding the annulus of fluid 2 is an infinite fluid medium denoted fluid 3. The interface between fluids 1 and 2 is denoted interface 1, and the interface between fluids 2 and 3 is denoted interface 2. A cross section of this arrangement is shown in Figure 8.

With reference to a fuel-air cloud, fluid 1 represents the detonation reaction product gases for the high explosive burster charge. Fluid 2 represents the liquid fuel to be dispersed. Fluid 3 represents the ambient atmosphere.

Let

- $\rho$ represent fluid density,
- R represent the radial spatial variable,
- t represent time,
- U represent the radial velocity component, and
- P represent pressure.

We non-dimensionalize using the following scales:

- $z_\emptyset$ for length,
- $V_o$ for velocity,
- $z_\emptyset/V_o$ for time, and
- $(\rho_1 + \rho_2 + \rho_3)V_o^2$ for pressures and pressure differences.

We also define the density ratios $\beta_i = \rho_i/(\rho_1 + \rho_2 + \rho_3)$.

This produces the non-dimensional variables:

- r for radius
- $\tau$ for time
- u for the radial velocity component, and
- p for pressure

given in Table 1.

We assume that the fluid in the film is inviscid and incompressible, and the flow is purely radial, isochoric, irrotational, and isothermal.

Equivalently, we can assume that the flow is purely radial, the Mach number $M \rightarrow 0$, the Reynolds number $R_e \rightarrow \infty$, and the Prandtl number $P_r \rightarrow 0$ (but in such a way that $R_e P_r \rightarrow \infty$).

Although these assumptions are not valid in the expanding detonation reaction product gases, or in the surrounding atmosphere, they permit an analytical solution to be obtained. Predictions from this solution will provide useful bounds on the liquid breakup time and the initial drop diameter. The predicted bounds can then be compared to the experimental data.

The basic motions of the inner and outer interfaces are prescribed by $r_i(\tau)$ and $r_o(\tau)$, respectively, with

$$r_i(\tau) \; \dot{r}_i(\tau) = r_o(\tau) \; \dot{r}_o(\tau)$$

where the overdot indicates differentiation with respect to $\tau$. This relation is a consequence of the assumption of isochoric flow.

The basic motions are then perturbed by small amounts $\eta_i Y_m Z_n$ to

$$r_1(\tau) = r_i(\tau) + \eta_1(\tau) \; Y_m Z_n \qquad \text{(inner interface)}$$

$$r_2(\tau) = r_o(\tau) + \eta_2(\tau) \; Y_m Z_n \qquad \text{(outer interface)}$$

where $\quad Y_m = A_m \cos(m\theta) + B_m \sin(m\theta)$, and $Z_n = \cos(n\pi z)$.

$A_m$ and $B_m$ are constants. The index n specifies the axial mode; the index m specifies the polar (or circumferential) mode.

We have assumed here that the indices (m, n) are the same for both interfaces. It can be shown by repeating this entire analysis with different indices for each interface that the only solutions with different values of the indices for each interface are trivial ones.

Hence it is valid to assume that the indices are the same for both interfaces.

Under these conditions, the equations of motion in the three fluids admit a solution in terms of a velocity potential $\phi_i$ in each fluid, such that

$$\nabla_2 \phi_i = 0 \quad \text{and} \quad \vec{v} = \nabla \phi_i \quad .$$

$\nabla$ is the vector gradient operator, and $\nabla^2$ is the Laplacian.

As boundary conditions, we require that the normal velocities of the fluids be equal at the appropriate interfaces:

$$\vec{n}_1 \cdot \nabla \phi_1 = \vec{n}_1 \cdot \nabla \phi_2 \quad \text{and} \quad \vec{n}_2 \cdot \nabla \phi_2 = \vec{n}_2 \cdot \nabla \phi_3$$

$\vec{n}_i$ is a unit normal to interface i.

We follow the method used by Plesset [25]. In Fluid 1, we find that, to first order in $\eta_i$, $\phi_1$ is given by

$$\phi_1 = r_i(\tau)\, \dot{r}_i(\tau)\, \ln r + \left[ \frac{\dot{\eta}_1}{\eta_1} + \frac{\dot{r}_i(\tau)}{r_i(\tau)} \right] \frac{I_m(kr)}{k\, I_m{}'(kr_i)}\, Y_m Z_n \quad ,$$

$$0 < r < r_i(\tau), \text{ and } k = n\pi.$$

$I_m$ is the modified Bessels function of the first kind of order m. A prime denotes differentiation with respect to the argument (kr in this case).

In Fluid 3, we find that, to first order in $\eta_i$, $\phi_3$ is given by

$$\phi_3 = r_o(\tau)\, \dot{r}_o(\tau)\, \ln r + \left[ \frac{\dot{\eta}_2}{\eta_2} + \frac{\dot{r}_o(\tau)}{r_o(\tau)} \right] \frac{K_m(kr)}{k\, K_m{}'(kr_o)}\, Y_m Z_n \quad ,$$

$$r_o(\tau) < r_i < \infty \quad .$$

$K_m$ is the modified Bessels function of the second kind of order m.

In the film, we find that, to first order in $\eta_i$, $\phi_2$ is given by

$$\phi_2 = r_o(\tau) \; \dot{r}_o(\tau) \ln r + \eta_1 Y_m Z_n \left[\frac{\dot{\eta}_1}{\eta_1} + \frac{\dot{r}_i}{r_i}\right] Q_1 + \eta_2 Y_m Z_n \left[\frac{\dot{\eta}_2}{\eta_2} + \frac{\dot{r}_o}{r_o}\right] Q_2 \quad ,$$

$$Q_1 = \frac{I_m(kr) \; K_m{}'(kr_o) - I_m{}'(kr_o) \; K_m(kr)}{k\left[I_m{}'(kr_i) \; K_m{}'(kr_o) - I_m{}'(kr_o) \; K_m{}'(kr_i)\right]} \quad ,$$

$$Q_2 = \frac{I_m(kr) \; K_m{}'(kr_i) - I_m{}'(kr_i) \; K_m(kr)}{k\left[I_m{}'(kr_o) \; K_m{}'(kr_i) - I_m{}'(kr_i) \; K_m{}'(kr_o)\right]} \quad .$$

Using Bernoulli's principle,

$$\frac{\partial \phi_i}{\partial \tau} + \frac{1}{2} \left(\nabla \phi_i\right)^2 + \frac{p_i}{\beta_i} = c_i(\tau)$$

in each fluid, and the interface conditions

$$P_{1+} = P_{1-} - \frac{1}{W_{e1}} \left\{ \frac{1}{r_i} - \frac{\eta_1}{r_i{}^2} \left(Y_m Z_n + Y_m{}'' Z_n - Y_m Z_n{}''\right) \right\}$$

$$P_{2+} = P_{2-} - \frac{1}{W_{e2}} \left\{ \frac{1}{r_o} - \frac{\eta_2}{r_o{}^2} \left(Y_m Z_n + Y_m{}'' Z_n - Y_m Z_n{}''\right) \right\}$$

where $We_i = (\rho_1 + \rho_2 + \rho_3)V_o{}^2 z_\beta/\sigma_i$ is the Weber number of interface i, and $p_{i\pm}$ is the pressure just inside (-) interface i or just outside (+) interface i, we find that, to zeroth order in $\eta_i$,

- 53 -

$$(\beta_2 - \beta_1)\left\{\ln(r_i)\ \frac{d}{d\tau}\left(r_i\dot{r}_i\right) + \frac{1}{2}\ \dot{r}_i^2\right\} = \beta_2 c_2(\tau) - \beta_1 c_1(\tau) + \frac{1}{r_i W_{e1}}$$

$$(4.1)$$

$$(\beta_3 - \beta_2)\left\{\ln(r_o)\ \frac{d}{d\tau}\left(r_o\dot{r}_o\right) + \frac{1}{2}\ \dot{r}_o^2\right\} = \beta_3 c_3(\tau) - \beta_2 c_2(\tau) + \frac{1}{r_o W_{e2}}$$

$$(4.2)$$

These equations relate $r_i$ and $r_o$ to the functions $c_i(\tau)$. We will assume that, given functions $r_i(\tau)$ and $r_o(\tau)$, we can find functions $c_i(\tau)$ consistent with (4.1) and (4.2).

To first order in $\eta_i$, we have

$$\frac{d}{d\tau}\left(r_i f_{11}\dot{\eta}_1\right) - G_1\eta_1 - r_i \frac{d}{d\tau}\left[\frac{f_{12}}{r_o}\frac{d}{d\tau}\left(r_o\eta_2\right)\right] = 0 \qquad (4.3)$$

$$\frac{d}{d\tau}\left(r_o f_{22}\dot{\eta}_2\right) - G_2\eta_2 + r_o \frac{d}{d\tau}\left[\frac{f_{21}}{r_o}\frac{d}{d\tau}\left(r_o\eta_1\right)\right] = 0 \qquad (4.4)$$

where

$$G_1 = (\beta_2 - \beta_2)\ r_i r_i - r_i \frac{d}{d\tau}\left[\frac{\dot{r}_i}{r_i}\ f_{11}\right] + \frac{1}{r_i W_{e1}}\left[1 - m^2 - kr_i\right)^2\right]$$

$$G_2 = (\beta_3 - \beta_2)\ r_o r_o - r_o \frac{d}{d\tau}\left[\frac{\dot{r}_o}{r_o}\ f_{22}\right] + \frac{1}{r_o W_{e2}}\left[1 - m^2 - kr_o\right)^2\right]$$

$$f_{11} = \frac{\beta_1}{k}\ \frac{I_m(kr_i)}{I_m'(kr_i)} - \frac{\beta_2}{k}\ \frac{I_m(kr_i)\ K_m'(kr_o) - I_m'(kr_o)\ K_m(kr_i)}{I_m'(kr_i)\ K_m'(kr_o) - I_m'(kr_o)\ K_m'(kr_i)}$$

$$f_{12} = \frac{\beta_2}{k}\ \frac{I_m(kr_i)\ K_m'(kr_i) - I_m'(kr_i)\ K_m(kr_i)}{I_m'(kr_o)\ K_m'(kr_i) - I_m'(kr_i)\ K_m'(kr_o)}$$

$$f_{21} = \frac{\beta_2}{k} \; \frac{I_m(kr_o) \; K_m{}'(kr_o) \; - \; I_m{}'(kr_o) \; K_m(kr_o)}{I_m{}'(kr_i) \; K_m{}'(kr_o) \; - \; I_m{}'(kr_o) \; K_m{}'(kr_i)}$$

$$f_{22} = - \frac{\beta_3}{k} \; \frac{K_m(kr_o)}{K_m{}'(kr_o)} \; + \; \frac{\beta_2}{k} \; \frac{I_m(kr_o) \; K_m{}'(kr_i) \; - \; I_m{}'(kr_i) \; K_m(kr_o)}{I_m{}'(kr_o) \; K_m{}'(kr_i) \; - \; I_m{}'(kr_i) \; K_m{}'(kr_o)}$$

Equations (4.3) and (4.4) resemble a Sturm-Liouville system. However, owing to the coupling between $\eta_1$ and $\eta_2$, it is not possible to assert a *priori* that the solutions are stable if the functions $G_i$ are negative, nor that the solutions are linearly unstable if the functions $G_i$ are positive. (This is because examples of such systems exist which violate this.)

Equations (4.3) and (4.4) reduce to the appropriate result for a single interface in the limit $r_i \to r_o$, and to the classical result for an infinite plane layer in the limit $r_i \to \infty$, $r_o \to \infty$, $r_i < r_o$ [26].

Equations (4.3) and (4.4), with appropriate initial conditions, $\eta_i(0)$ and $\eta'_i(0)$, can be integrated numerically, and the behavior of the solutions determined for various values of $\beta_i$, various disturbances (m, n), and various functions $r_o(\tau)$. Cases of interest in the explosive dispersal of liquids include:

- $\beta_2 > \beta_1, \; \beta_3$,

- $\beta_1 > \beta_2 > \beta_3$,

- constant velocity expansion,
- decelerating expansion, and
- accelerating-decelerating expansion.

We restrict our attention to (dimensional) functions $R_o(\tau)$ of the form

$$R_o(t) = R_\infty \{ 1 - \exp[-a(t + t_\emptyset)] \}$$

which represents a reasonable approximation, based on cloud growth data for typical fuel-air explosive clouds. $R_\infty$ is the fully-expanded, equilibrium cloud radius, $a$ is a time constant, and $t_\emptyset$ is a constant, determined from

$$R_o(0) = R_\infty\{ 1 - \exp[-\alpha t_\emptyset]\}.$$

In dimensionless variables,

$$r_o(\tau) = r_\infty\{ 1 - \exp[-\alpha^*(\tau + \tau_\emptyset)]\}$$

where $\alpha_* = z_\emptyset/R_\infty$ and $r_\infty = R_\infty/z_\emptyset$. A convenient velocity scale is then $V_o = \alpha R_\infty$.

To use the model, we can predict the breakup time and initial drop dia-meter from the time when the amplitude of the instabilities equals the thickness of the film, for some appropriate initial conditions $\eta_i(0)$ and $\eta_i(0)$, i.e., the breakup time $\tau_b$ is the time when

$$\max\left\{\left|\eta_1(\tau_b)\right| , \left|\eta_2(\tau_b)\right|\right\} = r_o(\tau_b) - r_i(\tau_b) = w(\tau_b)$$

and the initial drop diameter is predicted to be $w(\tau_b)$.

The model is formally valid only when $|\eta_i|$ is very much less than one. From the construction of the physical device, the amplitudes of initial disturbances are expected to be small, on the order of a millimeter or so. Thus a practical limit is $|\eta_i(0)|z_\emptyset \leq 1$ mm. So for computational purposes we take

$$|\eta_i(0)| \leq \max\{\min\{0.01, (1.0 \text{ mm})/z_\emptyset\}, 0.01\}.$$

Similarly, there are bounds on the velocities $\dot{\eta}_i(0)$. A practical limit is disturbance velocities on the order of one meter per second; thus

$$|\dot{\eta}_i(0)| \leq \max\{\min\{0.01, (1.0 \text{ m/sec})/(\alpha R_\infty)\}, 0.01\}$$

where $\alpha R_\infty$ is the velocity scale.

As noted above, the linear stability model is valid only for $|\eta_i(\tau)|$ very much less than one. To predict the breakup time and the initial arithmetic average drop diameter, it is necessary to violate this criterion; i.e., to use the linear model in a flow regime where a nonlinear model is required. This means that the predicted breakup time will be too small, and the predicted initial arithmetic average drop diameter will be too large.

The predicted breakup time is too small because the growth rate of these instabilities is known to decrease in the nonlinear regime [21]. Consequently, the estimates of the breakup time made with the linear model will underestimate the breakup time.

The predicted initial arithmetic average drop diameter will be too large because in the nonlinear regime the small-scale components of the evolving disturbance grow faster than the large-scale ones [21]. Thus the disturbance modes that cause the breakup will be smaller (i.e., will have larger values of n and/or m) than the critical ones indicated by the linear model. Hence the breakup will produce smaller initial arithmetic average drop diameters than those indicated by the linear model.

However, the model can be used to place a useful lower bound on the breakup time and an upper bound on the initial drop diameter.

In addition, since the initial conditions are unknown, we can take the largest permissible values of $|\eta_i(0)|$ and $|\dot{\eta}_i(0)|$ to produce the fastest growing disturbances (in the linear model) and hence the earliest estimated breakup time and the largest estimated initial arithmetic average drop diameter.

Predictions from the model can be compared to the measured breakup time and initial drop diameter reported by Samirant $et$ $al.$ [12] for a device in which $z_\emptyset = 6.0$ cm, $R_o(0) = 5.5$ cm, and $R_i(0) = 1.5$ cm. Using the velocity data presented in [12], $R_\infty = 184.10$ cm, $t_\emptyset = 0.020641$ msec, and $a = 1.4695$/msec; thus $a^* = 0.032591$, $r_\infty = 30.683$, $\tau_\emptyset = 0.93069$, and

$$r_o(\tau) = 30.683 \ \{1 - \exp[-0.032591(\tau + 0.93069)]\}$$

The initial conditions used for integrating (4.3) and (4.4) were $\eta_1(0) = -0.01$, $\eta_2(0) = \dot{\eta}_1(0) = \dot{\eta}_2(0) = 0$. The evolution of $\eta_i$ and $w(\tau)$ is shown in Figure 9. Numerical results are given in Table 2.

As expected, the estimated breakup time is less than the measured breakup time. The estimated initial arithmetic average drop diameter is slightly less than the measured drop diameter. However, according to Samirant $et$ $al.$ [12], immediately prior to breakup the film thickness was 3 mm, and immediately after breakup the arithmetic average drop diameter was 5 mm. This suggests that the linear model slightly over-

estimates the film thickness at breakup, and that the initial arithmetic average drop diameter is approximately twice the film thickness just prior to breakup.

The conclusion is that the film instability model places a

- lower bound on the breakup time, and
- lower bound on the initial arithmetic average drop diameter.

We can obtain an upper bound on the initial arithmetic average drop diameter by taking

$$d \leq 2w(\tau_b).$$

where $w(\tau)$ is the dimensionless film thickness, and d is the dimensionless drop diameter.

To use the model, we estimate the breakup time and initial drop diameter from the time when the amplitude of the fastest growing instability (obtained by integrating (4.3) and (4.4) numerically) equals the thickness of the film, for initial conditions $\eta_i(0)$ and $\dot{\eta}_i(0)$ given by

$$|\eta_i(0)| = \max\{\min\{0.01, \ (1.0 \text{ mm})/z_\emptyset\}, \ 0.01\}$$

and

$$|\dot{\eta}_i(0)| = \max\{\min\{0.01, \ (1.0 \text{ m/sec})/(aR_\infty)\}, \ 0.01\},$$

where $aR_\infty$ is the velocity scale.

The breakup time $\tau_b$ is the time when

$$\max\{ \ |\eta_1(\tau_b)|, \ |\eta_2(\tau_b)| \} = r_o(\tau_b) - r_i(\tau_b) = w(\tau_b),$$

and the initial arithmetic average drop diameter d lies in the range

$$w(\tau_b) \leq d \leq 2w(\tau_b).$$

## Parameter Study of the Film Instability Model

The behavior of the film instability model was explored for a variety of cases of interest in the modeling of fuel-air explosives. Cases considered were

- various values of the indices n and m,
- various relative values of the density ratios $\beta_i$,
- various forms for the basic motion $r_o(\tau)$, and
- various values for the surface tensions $\sigma_i$.

The specific values for the results reported here are given in Table 7.

The definition of stability here is less restrictive than the usual mathematical definition of stability. Since the differential equations (4.3) and (4.4) are non-autonomous (i.e., the coefficients contain the time variable $\tau$ explicitly, via $r_o$ and $r_i$) the mathematical stability of the equations cannot be rigorously inferred from the eigenvalues. What is required in the film instability model is that the amplitude of some disturbance mode with indices (n, m) grow until it equals the thickness of the film. For example, an oscillating disturbance with constant amplitude, which is mathematically stable, will cause the breakup of the film when the film thins to the point where its thickness equals the amplitude of the oscillations. (This means that any non-damped disturbance will ultimately disrupt the film, as the film thins.)

In the film instability model, a radially expanding film is said to be (linearly) unstable if there exists one disturbance mode whose amplitude at some time equals or is greater than the thickness of the film at that time.

Table 7: Cases considered in exploring the behavior of the film instability model.

| Expansion Type | Density Ratios | Disturbance Indices (n,m) | Figure No. |
|---|---|---|---|
| Constant velocity $r_o(\tau) = 1 + \tau$ | $\beta_1 = 0,\ \beta_2 = 1,\ \beta_3 = 0$ | (1,0); (5,0); (1,5); (5,5) | 12 |
| | $\beta_1 = 0.66667,\ \beta_2 = 0.33333,\ \beta_3 = 0$ | (1,0); (5,0); (1,5); (5,5) | 13 |
| Constant acceleration $r_o(\tau) = 0.025\tau^2 + \tau + 1$ | $\beta_1 = 0,\ \beta_2 = 1,\ \beta_3 = 0$ | (1,0); (5,0); (1,5); (5,5) | 14 |
| | $\beta_1 = 0.66667,\ \beta_2 = 0.33333,\ \beta_3 = 0$ | (1,0); (5,0); (1,5); (5,5) | 15 |
| Constant deceleration $r_o(\tau) = -0.025\tau^2 + \tau + 1$ | $\beta_1 = 0,\ \beta_2 = 1,\ \beta_3 = 0$ | (1,0); (5,0); (1,5); (5,5) | 16 |
| | $\beta_1 = 0.66667,\ \beta_2 = 0.33333,\ \beta_3 = 0$ | (1,0); (5,0); (1,5); (5,5) | 17 |
| Acceleration-deceleration $r_c(\tau) = -0.016667\tau^3 + 0.025\tau^2 + \tau + 1$ | $\beta_1 = 0,\ \beta_2 = 1,\ \beta_3 = 0$ | (1,0); (5,0); (1,5); (5,5) | 18 |
| | $\beta_1 = 0.66667,\ \beta_2 = 0.33333,\ \beta_3 = 0$ | (1,0); (5,0); (1,5); (5,5) | 19 |

Note: In all cases, $W_{ei} = \infty (\sigma_i = o)$ and the initial dimensionless film thickness $w(0) = 0.5$.

It would be convenient to infer the mathematical stability of a given disturbance mode from the eigenvalues of (4.3) and (4.4). Although this cannot be done rigorously, the eigenvalues will be used to indicate the stability of the expanding film as usual: if any one of the eigenvalues has a positive real part, then the film is indicated as unstable by the eigenvalues. This is valid for two reasons:

- in all cases tested, if the film was unstable (as defined above), then there was at least one eigenvalue with a positive real part, and

- the conclusions drawn from the stability of the film are the same as those drawn from the stability of a radially expanding single interface, for which the eigenvalues do rigorously indicate the (mathematical) stability.

In using the film instability model, the primary interest lies in when the amplitude of a disturbance equals or exceeds the thickness of the film. Thus the quantitative predictions made by the model are unaffected by the definition of stability. However, in order to understand the general behavior of a radially expanding fluid film, it is convenient to examine the eigenvalues. In this context, the critical eigenvalue is the one with largest real part.

Plots of the largest eigenvalue for representative cases from Table 7 are given in Figures 12-19.

Figures 12-13 show the real part of the critical eigenvalue for various combinations of the disturbance indices (n, m) and for a constant velocity radial expansion, and for two different combinations of the density ratios $\beta_i$ of interest in the dispersal of liquid fuels. Since the real part of the critical eigenvalue is always positive in these plots, we can infer that, even when there is no acceleration, radially expanding fluid films are unstable.

Figures 14-15 show the real part of the critical eigenvalue for various combinations of the disturbance indices (n, m) and for a constant-acceleration radial expansion, for two different combinations of the density ratios $\beta_i$. Since the real part of the critical eigenvalue is always ultimately positive in these plots, we can infer that accelerating, radially expanding films are unstable. A similar result holds for decelerating films (Figures 16-17).

- 61 -

Figures 18-19 show the real part of the critical eigenvalue for various combinations of the disturbance indices (n, m) and for an accelerating-density ratios $\beta_i$. Since the real part of the critical eigenvalue is always positive in these plots, we can infer that accelerating-decelerating, radially expanding films are unstable.

From Figures 12-19, we can also infer that, as a general rule, the (n, m) = (1, 0) disturbance is the most dangerous, i.e., grows most rapidly, because in most of the cases shown, its critical eigenvalue has the largest real part.

Although not shown in the figures, in some cases the critical eigenvalue is a complex conjugate pair, indicating an oscillatory disturbance with growing amplitude.

The effect of adding surface tension is to decrease the amplitudes of the disturbances $\eta_i$. This delays the film breakup, but does not prevent it: the films are always ultimately unstable. The concomitant predicted arithmetic mean drop diameter is thus decreased. This is illustrated by the predicted film breakup times and concomitant predicted drop diameters shown in Table 8. The results in the table are for

$$r_o(\tau) = r_\infty \{1 - \exp[-a^*(\tau + \tau_\beta)]\}$$

with $r_\infty = 21$, $a^* = 0.05$, $\tau_\beta = 0.97589$, $w(0) = 0.5$ (these values give the same initial conditions as those for the $r_o(\tau)$ functions listed in Table 7); $\beta_1 = \beta_3 = 0$, $\beta_2 = 1$; (n,m) = (1,0); and $\eta_1(0) = 0.01$, $\eta_2(0) = 0.01$, $\dot{\eta}_1(0) = \dot{\eta}_2(0) = 0$. The Weber numbers were $W_{e1} = \infty$ (corresponding to zero surface tension) and various values of $W_{e2}$. Decreasing $W_{e1}$, and $W_{12}$ (which corresponds to increasing surface tension) for this form of $r_o(\tau)$ produce relatively small decreases in the critical eigenvalue; the real part of the critical eigenvalue remains positive, indicating that the films are unstable. Changes in the functions $G_i$ with decreases in the Weber numbers are more pronounced, and are manifested in the behavior of $\eta_2(\tau)$. This behavior is illustrated in Figure 20. For $W_{e2} = \infty$, $\eta_2$ increases monotonically and rapidly; while for $W_{e2} = 500$, $\eta_2$ increases more slowly and oscillates.

In summary, examination of typical values for $\beta_i$ and typical expressions for $r_o(\tau)$ indicate that, in the absence of surface tension

- Radially expanding films are inherently unstable: there always exist modes which are amplified, even for a constant velocity expansion.

- The instability may be oscillatory: the amplitudes behave like $\exp(\lambda t)$, where $\text{Im}\{\lambda\}$ may be non-zero.

- Disturbances with smaller values of n and m tend to be more unstable than those with larger values.

Adding surface tension tends to stabilize the films, but does not eliminate the instability.

Table 8: Effect of surface tension on the breakup time and initial arithmetic average drop diameter predicted by the film instability model ($W_{e1} = \infty$; $d_{b1} \leq d \leq d_{b2}$)

| Outer Interface Weber Number $W_{e2}$ | Dimensionless Breakup Time $t_b$ | Dimensionless Drop Diameters | |
|---|---|---|---|
| | | $d_{b1}$ | $d_{b2}$ |
| 250 | 10.36 | 0.00414 | 0.00828 |
| 500 | 3.99 | 0.00820 | 0.0164 |
| 750 | 3.77 | 0.00854 | 0.0171 |
| 1000 | 3.68 | 0.00969 | 0.0174 |
| $\infty$ | 3.48 | 0.00905 | 0.0181 |
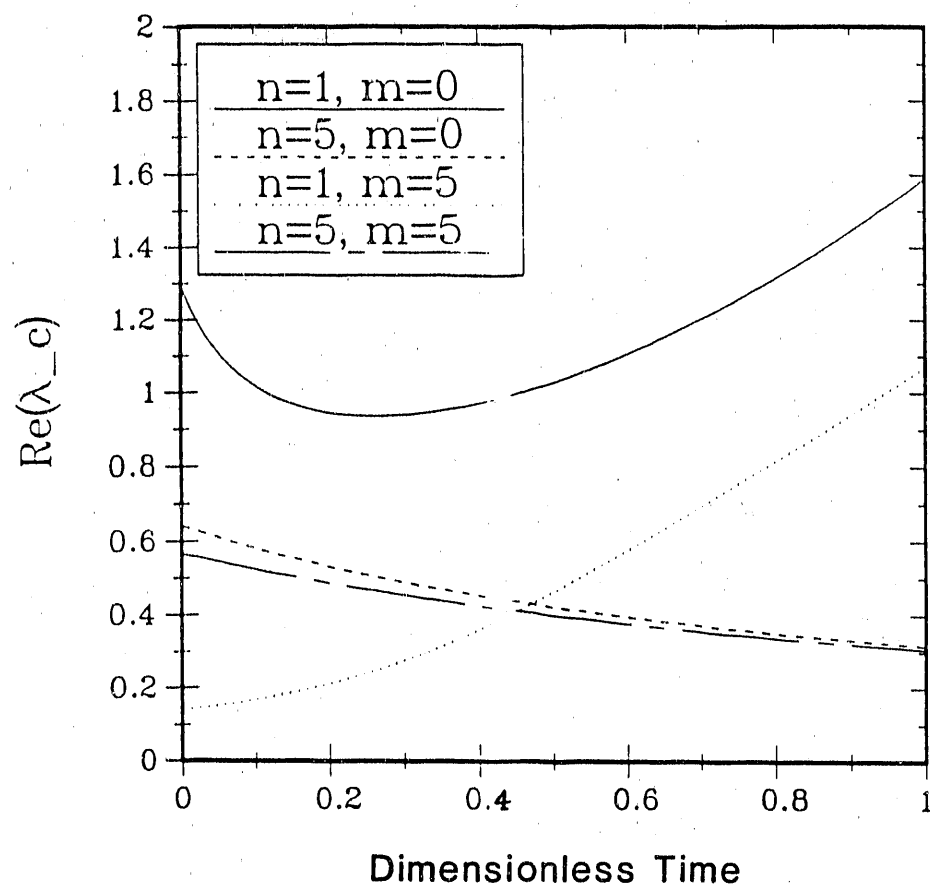
Figure 12: The real part of the most critical eigenvalue $\lambda_c$ for four different disturbances for a constant velocity radial expansion $r_o(\tau) = \tau + 1$, with density ratios $\beta_1 = 0$, $\beta_2 = 1$, and $\beta_3 = 0$.
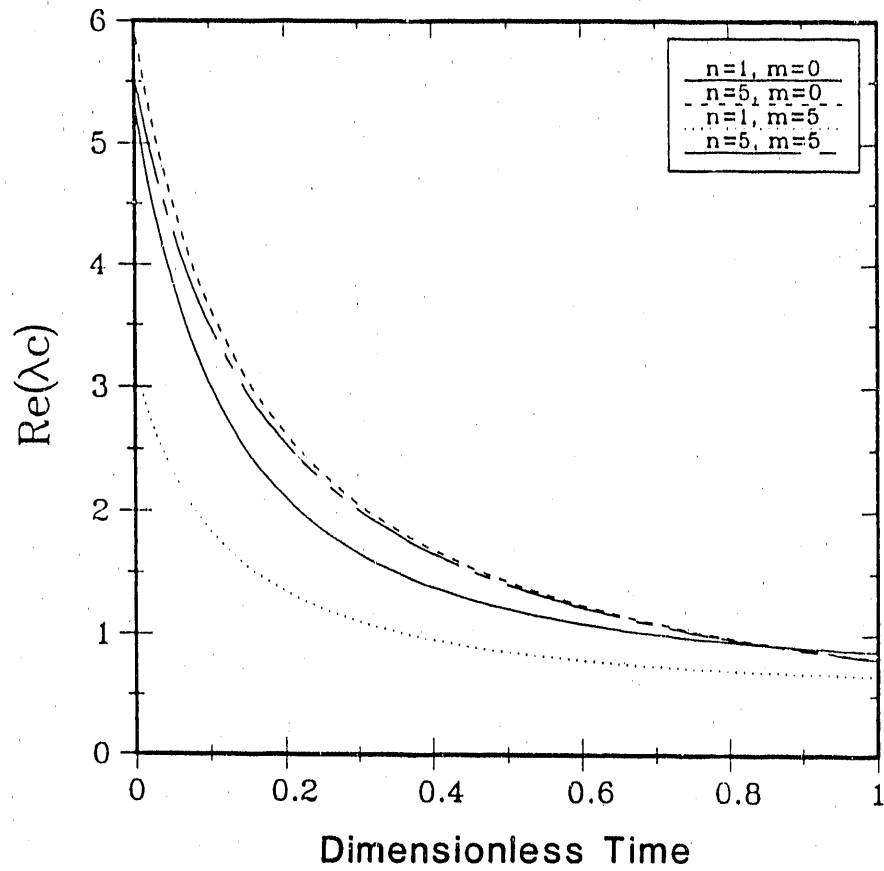
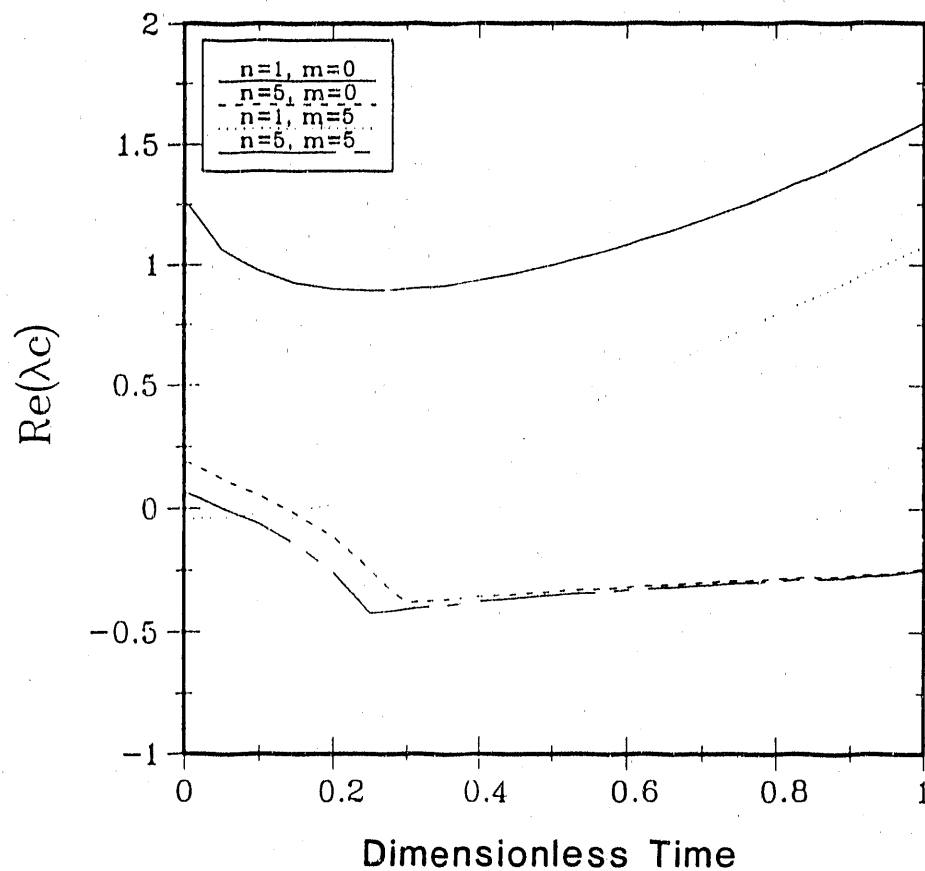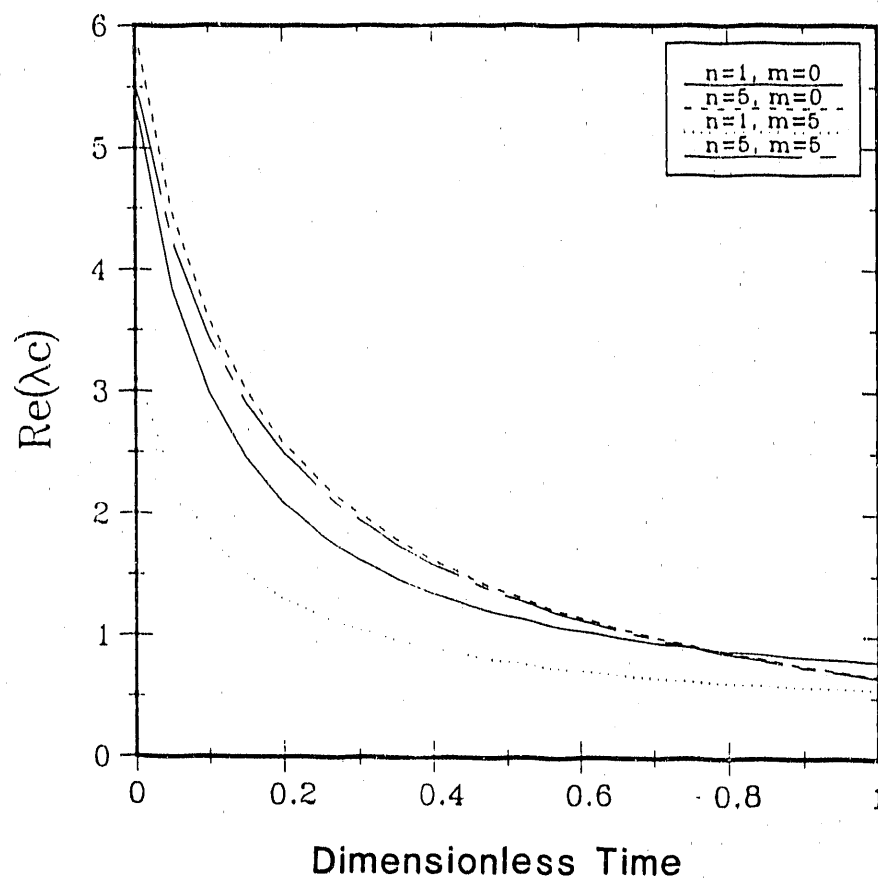Figure 13: The real part of the most critical eigenvalue $\lambda_c$ for four different disturbances for a constant velocity radial expansion $r_o(\tau) = \tau + 1$, with density ratios $\beta_1 = 0.66667$, $\beta_2 = 0.33333$, and $\beta_3 = 0$.

Figure 14: The real part of the most critical eigenvalue $\lambda_c$ for four different disturbances for a constant acceleration radial expansion $r_o(\tau) = 0.025\tau^2 + \tau + 1$, with density ratios $\beta_1 = 0$, $\beta_2 = 1$, and $\beta_3 = 0$.
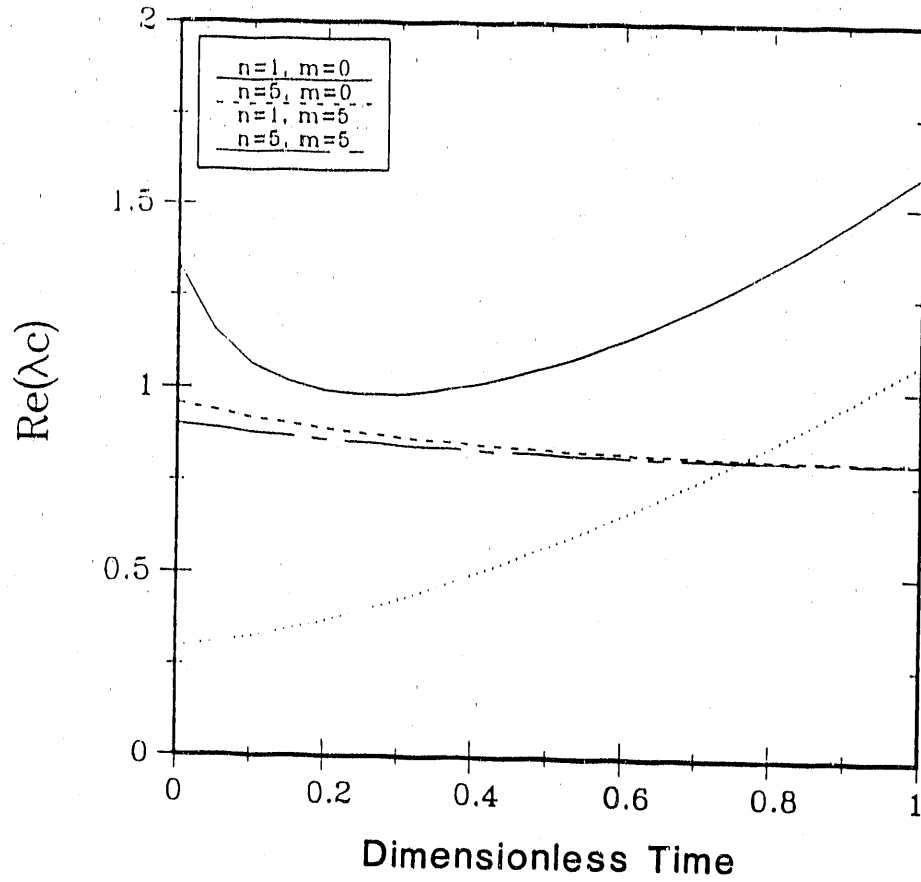
Figure 15: The real part of the most critical eigenvalue $\lambda_c$ for four different disturbances for a constant acceleration radial expansion $r_o(\tau) = 0.025\tau^2 + \tau + 1$, with density ratios $\beta_1 = 0.66667$, $\beta_2 = 0.33333$, and $\beta_3 = 0$.

Figure 16: The real part of the most critical eigenvalue $\lambda_c$ for four different disturbances for a constant deceleration radial expansion $r_o(\tau) = -0.025\tau^2 + \tau + 1$, with density ratios $\beta_1 = 0$, $\beta_2 = 1$, and $\beta_3 = 0$.
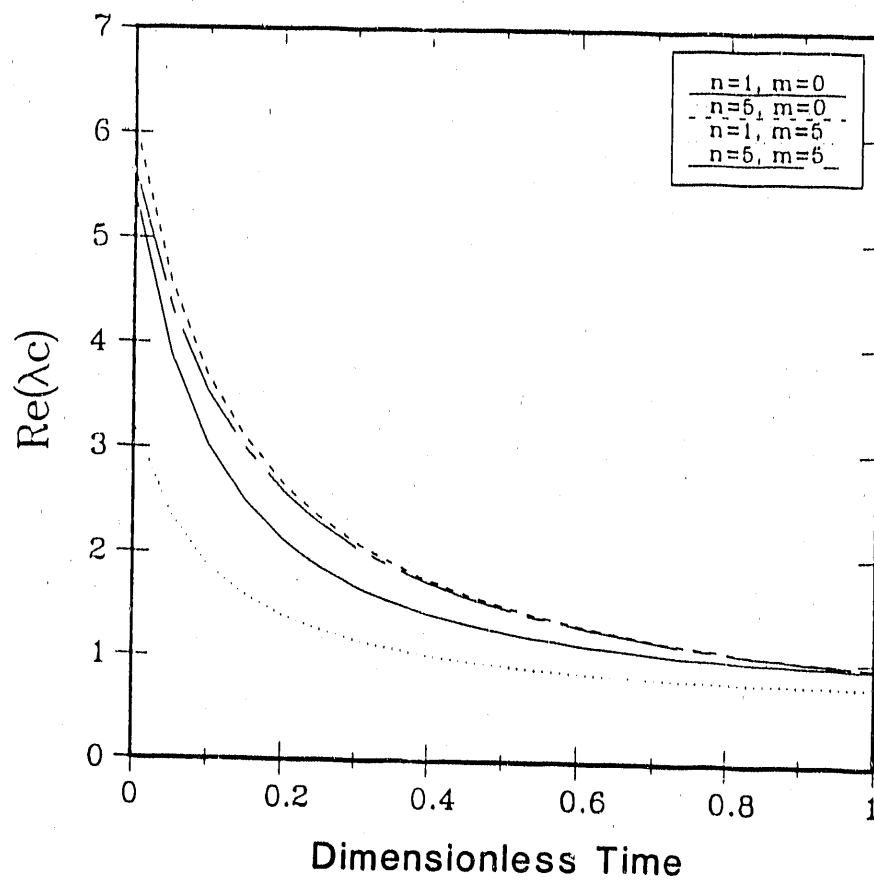
Figure 17: The real part of the most critical eigenvalue $\lambda_c$ for four different disturbances for a constant deceleration radial expansion $r_o(\tau) = -0.025\tau^2 + \tau + 1$, with density ratios $\beta_1 = 0.66667$, $\beta_2 = 0.33333$, and $\beta_3 = 0$.
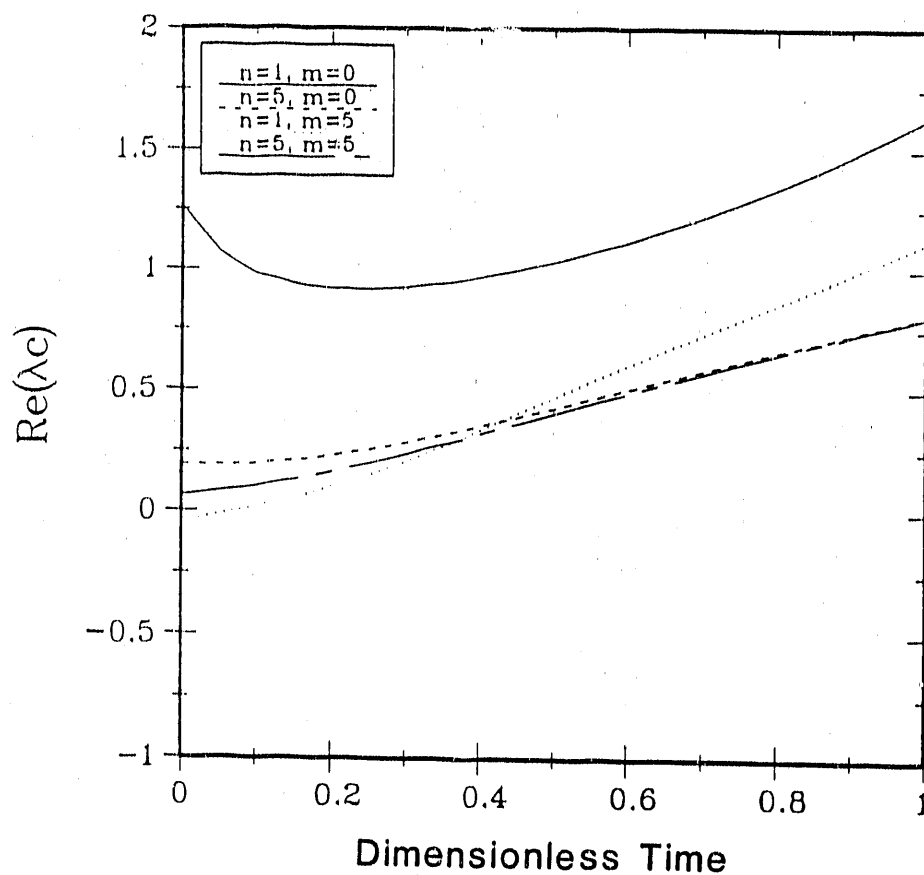
Figure 18: The real part of the most critical eigenvalue $\lambda_c$ for four different disturbances for a acceleration-deceleration radial expansion $r_o(\tau) = -0.016667\tau^3 + 0.025\tau^2 + \tau + 1$, with density ratios $\beta_1 = 0$, $\beta_2 = 1$, and $\beta_3 = 0$.
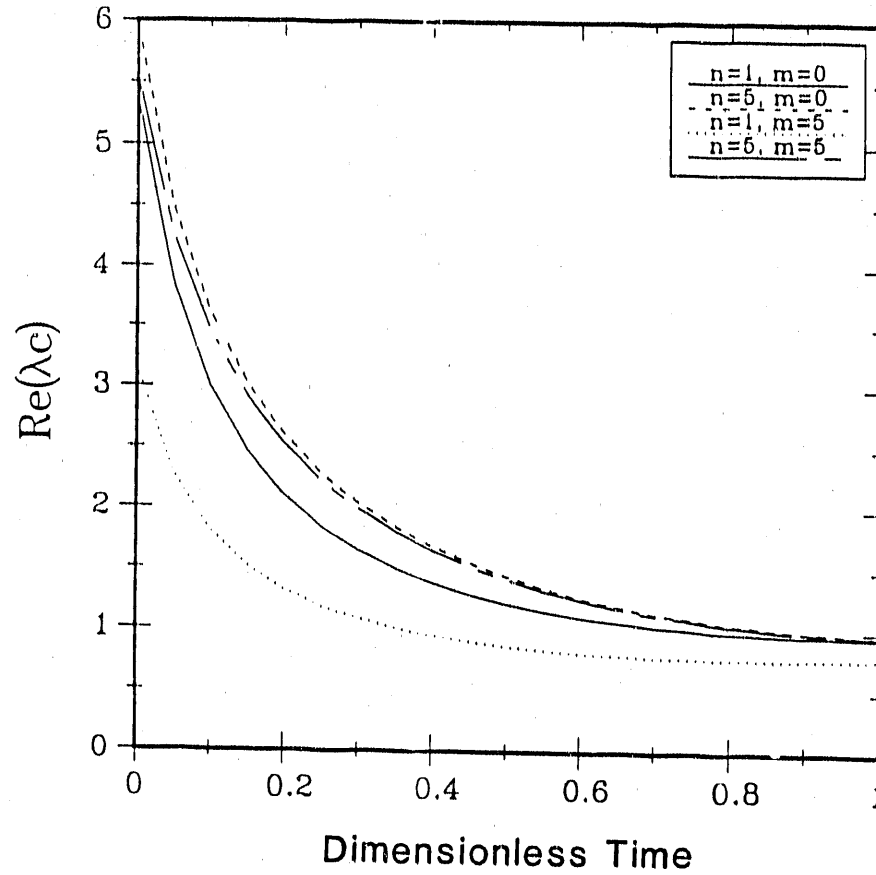
Figure 19: The real part of the most critical eigenvalue $\lambda_c$ for four different disturbances for a acceleration-deceleration radial expansion $r_o(\tau) = -0.016667\tau^3 + 0.025\tau^2 + \tau + 1$, with density ratios $\beta_1 = 0.66667$, $\beta_2 = 0.33333$, and $\beta_3 = 0$.
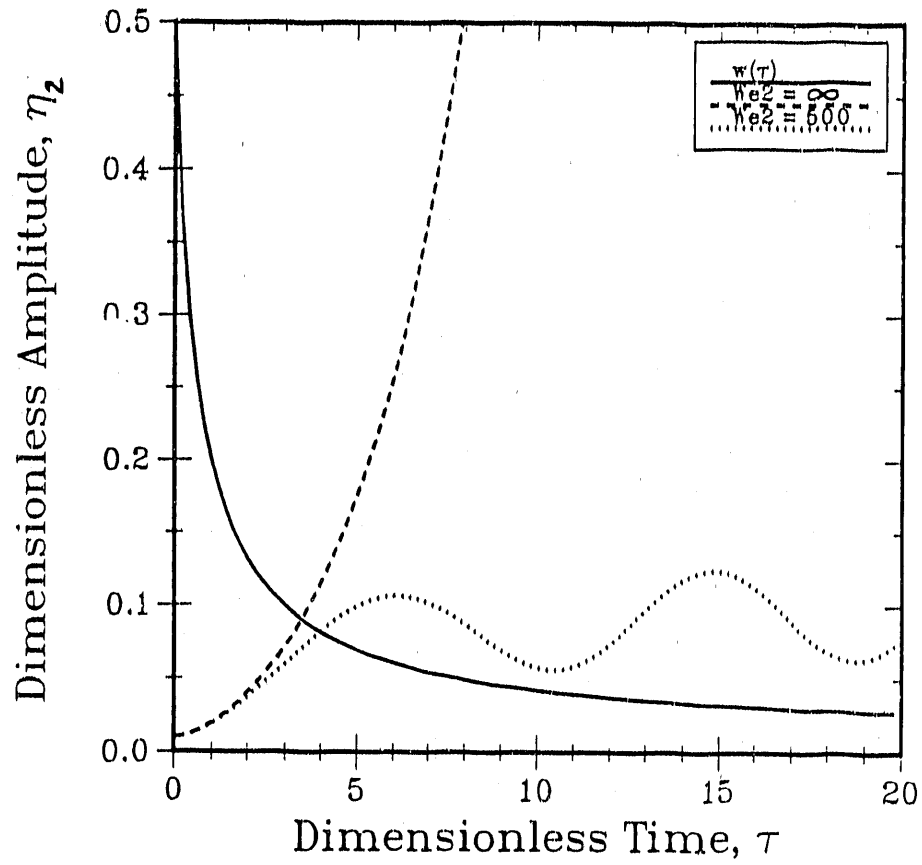
Figure 20: Evolution of the disturbance $\eta_2$ for different Weber numbers $W_{e2}$. Initial conditions are given in the text. w(t) is shown for reference.

# 6. REFERENCES

1. G. R. Abrahamson, R. W. Gates, G. M. Muller, K. Schreiner, ''Explosive Dissemination,'' SRI Technical Report No. 18, Special Report by Stanford Research Institute, Menlo Park, CA, for the Department of the Army, Edgewood Arsenal Research Laboratories (November 1977).

2. D. E. Buck, ''The explosive dissemination of liquids of low volatility,'' Army Chemical Warfare Laboratories, Army Chemical Center MD, CWL Special Publication-1-7, AD 312 068 (1959).

3. C. Kot, D. Morita, H. Nielson, H. Napadensky, R. Remaly, T. Stanley, A. Tulis, D. Werle, A. Wiedermann, ''Liquid Fuel-Air Explosive Technology Program. Volume I. Technical Discussion,'' AFATL-TR-72-224 (December 1972).

4. A. I. Ivandaev, A. G. Kutushev, R. I. Nigmatulin, ''Numerical investigation of the expansion of a cloud of dispersed particles or drops under the influence of an explosion,'' *Fluid Dynamics* 17, 68-74 (1982).

5. M. Rosenblatt, G. E. Eggum, K. N, Kreyenhagen, ''DICE-FAE analysis of fuel dispersal and detonation from a fuel-air-explosive device,'' Air Force Armament Laboratory Report AFATL-TR-76-33, March 1976.

6. W. H. Andersen, E. A. Lawson, ''Literature survey on explosive dissemination,'' Whittaker Corp., North Hollywood, CA, Shock Hydrodynamics Division, August 1979, AD-B042 944L.

7. A. A. Amsden, J. D. Ramshaw, P. J. O'Rourke, J. K. Dukovicz, ''KIVA: A computer program for two- and three-dimensional fluid flows with chemical reactions and fuel sprays,'' LA-10245-MS (1985).

8. A. A. Amsden, J. D. Ramshaw, L. D. Cloutman, P. J. O'Rourke, ''Improvements and extensions to the KIVA computer program,'' LA-10534-MS (1985).

9. A. A. Amsden, T. D. Butler, P. J. O'Rourke, and J. D. Ramshaw, ''KIVA: A comprehensive model for 2D and 3D engine simulations,'' SAE Technical Paper 850554 (1985).

10. A. A. Amsden, P. J. O'Rourke, T. D. Butler, ''KIVA-II: A computer program for chemically reactive flows with sprays,'' Los Alamos National Laboratory Report LA-11560-MS (May 1989).

11. W. H. Andersen, N. A. Louie, G. Ialongo, ''Investigation of the aerodynamic breakup of viscoelastic liquids. Phase I. Subsonic dissemination,'' Shock Hydrodynamics Division, Whittaker Corporation (North Hollywood, CA) for the US Army Armament Research and Development Command, Chemical Systems Laboratory, Aberdeen Proving Ground, MA, August 1977.

12. M. Samirant, G. Smeets, C. Baras, H. Royer, L. R. Oudin, ''Dynamic Measurements in Combustible and Detonable Aerosols,'' *Propellants, Explosives, Pyrotechnics* 14, 47-56 (1989).

13. L. B. Seely, J. G. Burke, ''Detonation, shock, and chemical reaction processes in explosive dissemination: Boundary stability and cavitation,'' SRI Technical Report No. 18, Special Report by Stanford Research Institute, Menlo Park, CA, for the Department of the Army, Edgewood Arsenal Research Laboratories (June 1967).

14. L. M. Sires, ''Holographic Measurement of FAE fuel droplet size,'' NWC TP 6043, Naval Weapons Center, China Lake, CA (February 1982).

15. J. M. McGlaun, F. J. Zeigler, S. L. Thompson, M. G. Elrick, ''CTH-User's manual and input instructions,'' SAND88-0523 (1988).

16. D. E. Grady, ''Local inertial effects in dynamic fragmentation,'' *J. Appl. Phys.* 53, 322-325 (1982).

17. D. E. Grady, ''Analysis of Prompt Fragmentation in Explosively Load Uranium Cylindrical Shells,'' Sandia National Laboratories Report SAND82-0140, February 1982.

18. D. E. Grady, T. K. Bergstresser, J. M. Taylor, ''Impact fragmentation of lead and uranium plates,'' SAND84-1545 (1985).

19. D. E. Grady, ''The spall strength of condensed matter,'' *J. Mech. Phys. Solids* 36, 353-384 (1988).

20. I. G. Poppoff, W. C. Thuman, ''Research studies on the dissemination of solid and liquid agents,'' Stanford Research Institute, Menlo Park, CA, Report AD 827272 (December 1967).

21. D. L. Youngs, ''Numerical simulation of turbulent mixing by Rayleigh-Taylor instability,'' *Physica* 12D, 32-44 (1984).

22. D. R. Gardner, M. W. Glass, ''A coupled near-field, far-field dispersal model for fuel-air explosives,'' Sandia National Laboratories Report SAND90-0687 (in preparation).

23. M. W. Glass, ''FAE far-field modeling,'' Sandia National Laboratories Report SAND90-0528, May 1990.

24. A. S. Geller, A. C. Ratzel, M. R. Baer, ''Application of a mixture theory model to the dispersal of solid by a high-pressure gas,'' Sandia National Laboratories Report SAND89-0512, April 1989.

25. M. S. Plesset, ''On the stability of fluid flows with spherical symmetry,'' *J. Appl. Phys.* 25, 96-98 (1954).

26. G. I. Taylor, ''The instability of liquid surfaces when accelerated in a direction perpendicular to their planes. I,'' *Proc. Roy. Soc.* A 201, 192-196 (1950).

# END

# DATE FILMED

10/29/90